

UNCLASSIFIED

AD 409274

DEFENSE DOCUMENTATION CENTER

FOR

SCIENTIFIC AND TECHNICAL INFORMATION

CAMERON STATION, ALEXANDRIA, VIRGINIA



UNCLASSIFIED

NOTICE: When government or other drawings, specifications or other data are used for any purpose other than in connection with a definitely related government procurement operation, the U. S. Government thereby incurs no responsibility, nor any obligation whatsoever; and the fact that the Government may have formulated, furnished, or in any way supplied the said drawings, specifications, or other data is not to be regarded by implication or otherwise as in any manner licensing the holder or any other person or corporation, or conveying any rights or permission to manufacture, use or sell any patented invention that may in any way be related thereto.

CATALOGED BY DDC

AS AD No. 409274

409274

SCRIPPS INSTITUTION OF OCEANOGRAPHY

UNIVERSITY OF CALIFORNIA

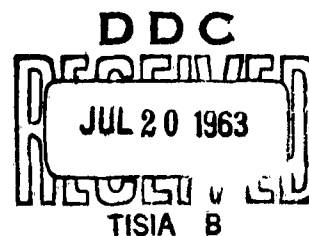
FINAL REPORT
Operation HYDRA II A

WATER WAVES FROM 10,000-LB HIGH-EXPLOSIVE CHARGES

sponsored by
Defense Atomic Support Agency
Office of Naval Research

Contract Nos Nonr 233(35),
Nonr 2216(15), Nonr 2216(16)

SIO Reference 63-20
1 June 1963



ERRATUM SHEET for

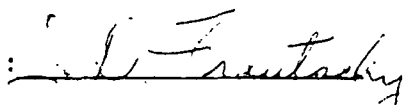
Scripps Institute of Oceanography Report 63-20, "Water Waves
from 10,000-lb High-Explosive Charges"

Figure 5.3, Page 62, Ordinate scale should cover range from
0.1 to 1.0 instead of from 1.0 to 10.0

WATER WAVES FROM 10,000-LB HIGH-EXPLOSIVE CHARGES
FINAL REPORT OPERATION HYDRA II-A
Contract Nonr 2216(15)

Wm. G. Van Dorn, Principal Investigator

W. S. Montgomery, Assoc. Engineer

Approved: 

for Director: Scripps Institution
of Oceanography

University of California
Scripps Institution of Oceanography
La Jolla, California

ABSTRACT

Water waves were recorded at three stations for eight out of thirteen 10,000 lb high-explosive charges detonated during the HYDRA IIA test program at San Clemente Island in the summer of 1961. The charge submergence varied from 6.6 to 140 ft in water 300 ft deep. Since the waves traveled over sloping topography, the theory of geometric optics was employed to reconstruct equivalent wave trains as they would have developed over a flat horizontal bottom in water 300 ft deep. The linear theory of Kranzer and Keller for the wave system initiated by a parabolic crater in the water was forced to fit the reconstructed HYDRA wave trains by suitably adjusting the input crater dimensions until the phase and amplitude of the predicted wave train was in good agreement with the reconstructed trains. This solution was then generalized to include the effect of variable charge weight in order to compare these results with those from a series of much smaller explosions. It was found that the theory, when normalized to a given experiment, adequately predicts the waves observed from explosions of widely differing charge weights and site geometries, when the charge depth of submergence is also scaled

inversely as the three-tenths power of charge weight. Comparison of the maximum waves produced by all tests on a scaled basis indicates that the effect of varying the charge submergence is quite complicated, the highest waves being produced by explosions at--or very near--the surface. The empirical curve which best fits the data has several maxima and minima, suggesting that the energy going into wavemaking is somehow linked to the phase of the explosion cavity as it reaches the water surface.

The total energy in wave motion computed from the linear theory is equal to the potential energy of the initial crater. For an explosion near the surface this energy represents about 2% of the available thermal energy of the charge.

PREFACE

Instrumentation and field work for the water waves studies carried out during the HYDRA II-A test series were supported by the Office of Naval Research under contract Nonr 2216(15). Data analysis and theoretical work were supported by the Defense Atomic Support Agency and the Office of Naval Research under contracts Nonr 233(35) and Nonr 2216(16).

CONTENTS

ABSTRACT	3
PREFACE	5
LIST OF SYMBOLS	9
CHAPTER 1 INTRODUCTION	13
1.1 Description of HYDRA II A	13
1.2 Objectives	13
1.3 Background	14
CHAPTER 2 EXPERIMENTAL PLAN	15
2.1 Layout	15
2.2 Instrumentation	15
2.2.1 Photo Instruments	17
2.2.2 Pressure Instrumentation	20
CHAPTER 3 RESULTS OF THE WAVE MEASUREMENTS	27
3.1 Shot Participation	27
3.2 Wave Results	27
CHAPTER 4 ANALYSIS OF RESULTS	35
4.1 Purpose of the Analysis	35
4.2 Calculation of the Phase Arrivals	37
4.3 Wave Amplitude Changes in Water of Variable Depth	40
4.4 Reconstruction of the Amplitude Spectrum of the Wave Train in Water of Constant Depth	46
4.5 The Equivalent Source	50
4.6 The Effect of Variable Charge Depth	52
CHAPTER 5 COMPARISON WITH OTHER TESTS	55
5.1 The Scaling Law for Variable Charge Weight	55
5.2 Determination of the Yield Exponents	56
5.3 Comparison of the Normalized Results	58
CHAPTER 6 DISCUSSION	65
6.1 Limitations of the Linear Solution	65
6.2 Wavemaking Efficiency	66
6.3 The Influence of Atmospheric Pressure	67
APPENDIX A DERIVATION OF THE WAVE INTENSITY EQUATION	69
REFERENCES	75

TABLES

3.1	Shot Participation and Geometry	28
4.1	Spectral Amplitudes and Energy Densities at Twelve Frequencies for Three Observation Stations	45
4.2	Spectral Amplitudes at Twelve Frequencies for Shot 11 Corrected to Uniform Water Depth $h = 300$ ft at Range $R = 1000$ ft	48
4.3	Maximum Spectral Amplitude at Various Charge Depths	48
5.1	Maximum Spectral Amplitude M and Associated Wave Number N as a Function of Reduced Charge Depth D	59

FIGURES

2.1	Geometry of the HYDRA II A test site, San Clemente Island	16
2.2	Schematic of photo-spar installation at Stations B and C	18
2.3	Mitchel Camera with 10-in lens used for spar photography	19
2.4	Block-diagram of camera activating circuit	21
2.5	Typical frame from spar camera	22
2.6	Detail of pressure transducer and protective case	23
2.7	Transducer installation at Station A	24
2.8	Block diagram of transducer electronics	26
3.1	Wave records from Station A (30 psi transducer)	29
3.2	Wave records from Station A (40 psi transducer)	30
3.3	Wave records from Station B	31
3.4	Wave records from Station C	32
4.1	Reconstructed wave envelope for Shot 11 at range $R = 1000$ ft in water depth $h = 300$ ft	49
5.1	Wave number and amplitude times range at amplitude maximum versus charge weight, for zero charge depth	60
5.2	Variation of maximum wave amplitude with charge depth at constant charge weight and range	61
5.3	Wave number at amplitude maximum versus charge depth at constant charge weight	62
A.1	Development of wave patch between two adjacent rays over arbitrary contours	70
A.2	Patch development for straight contours parallel to y axis	70

LIST OF SYMBOLS

SYMBOL	DESCRIPTION	UNITS ¹
a	Charge weight exponent (crater depth) (also subscript denoting atmospheric pressure)	
b	Charge weight exponent (crater radius)	
c	Wave phase velocity	ft/sec
d	Charge depth	ft
g	Gravitational acceleration	ft/sec ²
h	Water depth	ft
k	Wave number	ft ⁻¹
l	Wave number magnitude in x direction	ft ⁻¹
m	Wave number magnitude in y direction	ft ⁻¹
n	Phase order number or number of increments in summation	
o	Subscript referring to origin of coordinates or l-lb charge weight	
r	Polar distance coordinate	ft
s	Distance along a ray path	ft
t	Time unit	sec
x	Horizontal cartesian coordinate	ft
y	Horizontal cartesian coordinate	ft
z	Vertical cartesian coordinate	ft

¹ Units are given in MLT system unless numerical calculations are involved, in which case units are lb-ft-sec.

LIST OF SYMBOLS

SYMBOL	DESCRIPTION	UNITS
A	Wave station position (transducer)	
B	Wave station position (photo spar) (also charge weight ratio)	
C	Wave station position (photo spar)	
D	Reduced charge depth $D = d/B^b$	ft
E	Energy per unit frequency	ft-lb-sec
J_2	Bessel function of second order	
M	Reduced spectral amplitude maximum (η''_r/B^{a+b})	ft ²
N	Reduced wave number associated with M ($k''B^b$)	ft ⁻¹
O	Origin of coordinates centered on shot position	
P	Pressure	lb-ft ⁻²
R	Standard range (1000ft) for spectrum reconstruction	
V	Group velocity	ft/sec
W	Charge weight ($W_0 = 1\text{-lb}$)	lbs
Z	Wave intensity factor along refracted ray	ft ⁴ -sec

LIST OF SYMBOLS

SYMBOL	DESCRIPTION	UNITS
β	Function of group velocity $\beta = \frac{\partial}{\partial k} (1/V^2)$	$\text{sec}^2\text{-ft}^{-1}$
δ	Increment of distance in x direction	
ϵ	Analogue time parameter	L^2
η	Wave (or spectral) amplitude	ft
θ	Point of stationary phase	
ξ	Increment of patch length along a ray	
ρ	Density (of water)	lb-ft^{-3}
σ	Increment of patch width between adjacent rays	
ω	Spectral frequency	sec^{-1}
"	Exponent referring to spectral amplitude maximum	
'	Exponent referring to first spectral amplitude minimum	
\mathcal{H}	Hamiltonian function for water waves ($\mathcal{H} = gk \tanh kh$)	sec^{-1}

CHAPTER 1

INTRODUCTION

1.1 DESCRIPTION OF HYDRA II A

HYDRA II A was an experimental program dealing with the hydrodynamics of explosions in the sea, which was carried out on the southwest side of San Clemente Island during the summer of 1961. Planning and operations for the tests were under the direction of the U. S. Naval Radiological Defense Laboratory, San Francisco.

The original operation plan called for the firing of 18 charges of HBX-1 explosive each weighing 10,000 lbs. These were to be fired under identical test geometry with the only variable being the depth of charge submergence, although small shot to shot variations in the position of the firing site occurred under influence of varying current and weather conditions, as well as a gradual shift in the position of the charge downhaul clump.

Seasonal weather changes forced termination of the series after Shot 13. Details of charge design and handling can be found in Reference 1.

1.2 OBJECTIVES

The primary objective of participation in the HYDRA II A program by the Scripps Institution of Oceanography was the measurement and evaluation of water waves produced

by a series of large HE explosions at the same location, but over a wide range of charge depths, in order to evaluate a scaling function for charge depth which would be applicable to other geometries and charge weights. A second objective was to gather additional information on explosively generated waves on a scale several orders of magnitude larger than heretofore studied. The end objectives of all such experiments is, of course, the capability of predicting waves and wave effects for all cases of interest.

1.3 BACKGROUND

The HYDRA IIA series represents the largest yield group of tests yet conducted with chemical explosives where the study of water waves was an objective. Test results obtained by the Waterways Experiment Station dealt with shots in the $\frac{1}{2}$ -10 lb range, although WES has recently completed a test series with charge weights of 100 and 285 lbs. Thus the HYDRA IIA series extends the range of charge weights up into the lower range of nuclear tests, and far out of the range where such factors as atmospheric pressure can have an overweening influence on the early hydrodynamics of wave formation.

CHAPTER 2

EXPERIMENTAL PLAN

2.1 LAYOUT

Figure 2.1 shows the layout of the HYDRA experimental test facility at San Clemente. All tests were conducted in close proximity to point 0 (Surface Zero) in the figure, which was in 300 ft of water and about 2600 ft from shore. This area is particularly advantageous for wave observations because of the very-low ambient swell and wind wave background in the lee of the island. Wave measurements were conducted at three observation stations (A, B and C) along lines extending both inshore and offshore from the shot site. The bottom topography, which has an important influence on the nature of the wave development, was characterized by a gentle and fairly continuous slope from the shore to the 100-fathom contour. Although it would have been most advantageous to have located the wave stations along lines normal to the bottom contours, the station positions were to some extent influenced by the operational requirements of other measurement programs.

2.2 INSTRUMENTATION

Two types of instrumentation were used for wave

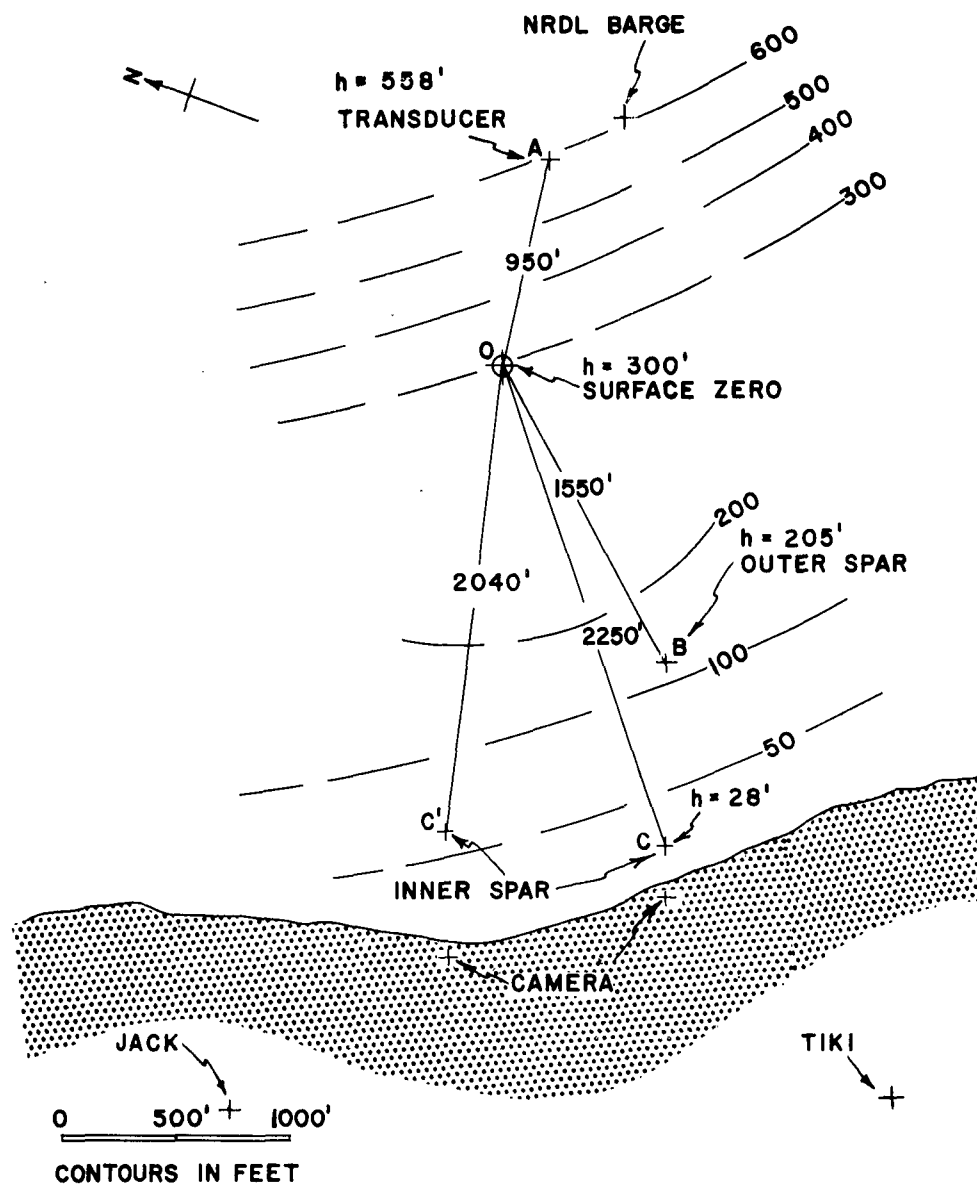


Figure 2.1 Geometry of the HYDRA II-A test site, San Clemente Island.

measurement; motion pictures of spars anchored in shallow water were taken from a camera station on shore, and subsurface (15 ft) pressure measurements were made in deep water beyond the shot site.

2.2.1 Photo Instruments. Figure 2.2 is a schematic of the photo spar installations at Stations B and C. A 15-ft length of 2-in diameter shelby tubing was painted with alternating white and red bands 1-ft in length, and mounted rigidly on the top of a standard Navy 28-in net float. This assembly, having about 150-lbs excess buoyancy, was submerged until the spar projected about half its length above the surface. The spars exhibited relatively little motion during these tests, and were never more than 10^0 from the vertical at any time. No attempt was made to correct the data for spar inclination.

To record the migration of the water surface up and down the striped spars, a Mitchel 35mm Photo-Triangulation Camera with a ten inch lens was located on the beach and oriented to include both spars in its field of view. Tests showed that this camera and lens when loaded with Anscochrome color film could resolve water migration of less than 0.1-ft at the maximum range used in this operation. (1100 ft) A photograph of the camera is shown in Figure 2.3.

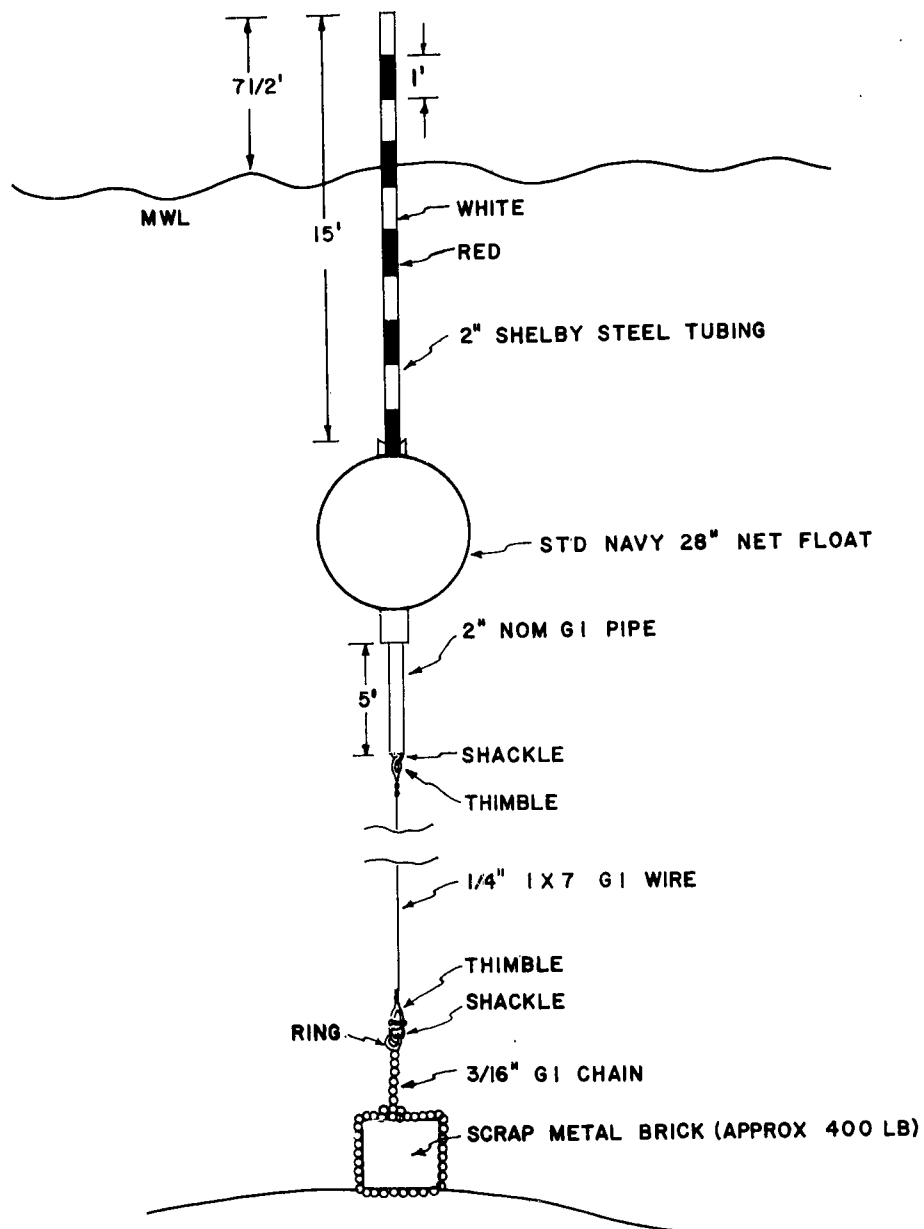


Figure 2.2 Schematic of photo-spar installation at Stations B and C.



Figure 2.3 Mitchell Camera with 10-in lens used for spar photography.

Safety requirements dictated that all personnel leave the beach at shot time. A controller-programmer was used to start the camera that depended only on a starting closure from the NRD L Master Programmer. A block diagram of the electrical circuitry is shown in Figure 2.4.

Fiduciary zero time was established by the blurred frames as the earth shock wave reached the camera location. Time control was established by a precision stop watch that was photographed in the margin of each data frame.

Readout was done on a Kodak Microfilm Reader. Each tenth frame was read except that where required enough frames were read to positively define the troughs and crests. The resolution of the readout was consistent with the overall resolution of 0.1 feet. A typical data frame is shown in Figure 2.5.

2.2.2 Pressure Instrumentation. The waves as they radiated to deeper water were beyond the range of stably mounted cameras, so Station A was equipped with two Statham absolute pressure transducers[~] (0-30 and 0-40 psia) encased and protected from shock pressure as shown in Figure 2.6. These transducers were also mounted on a taut-wire mooring as shown in Figure 2.7. The transducers were excited by an 1.1-KC carrier, and the modulated

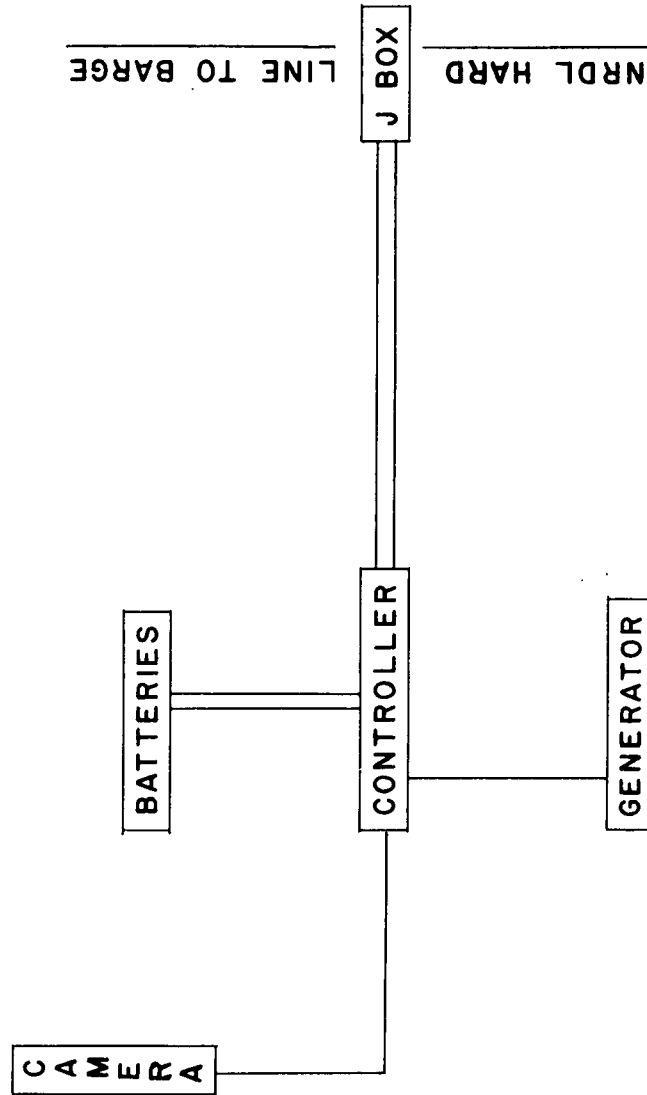


Figure 2.4 Block-diagram of camera activating circuit.

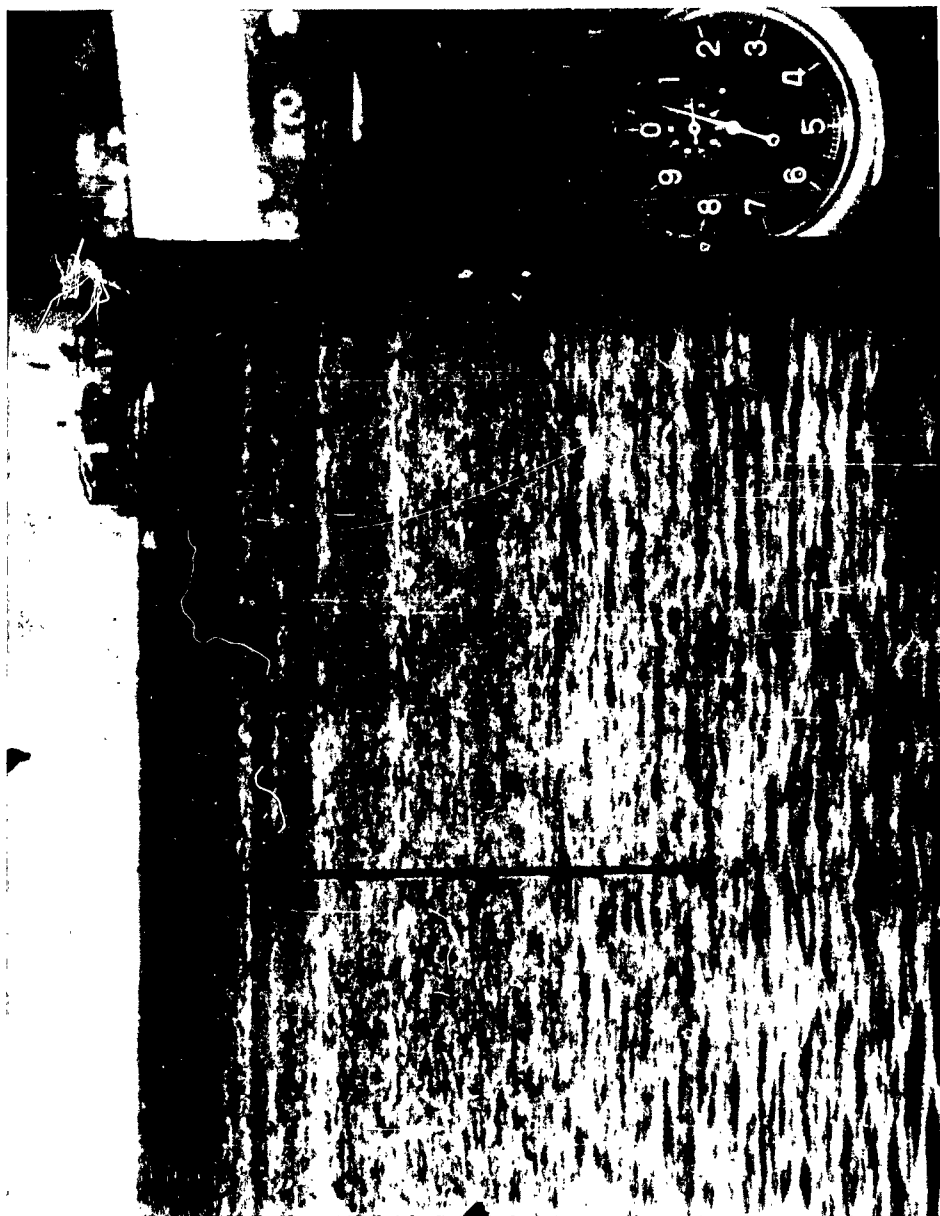


Figure 2.5 Typical frame from spar camera.
Farther spar was at about 1000-ft range.

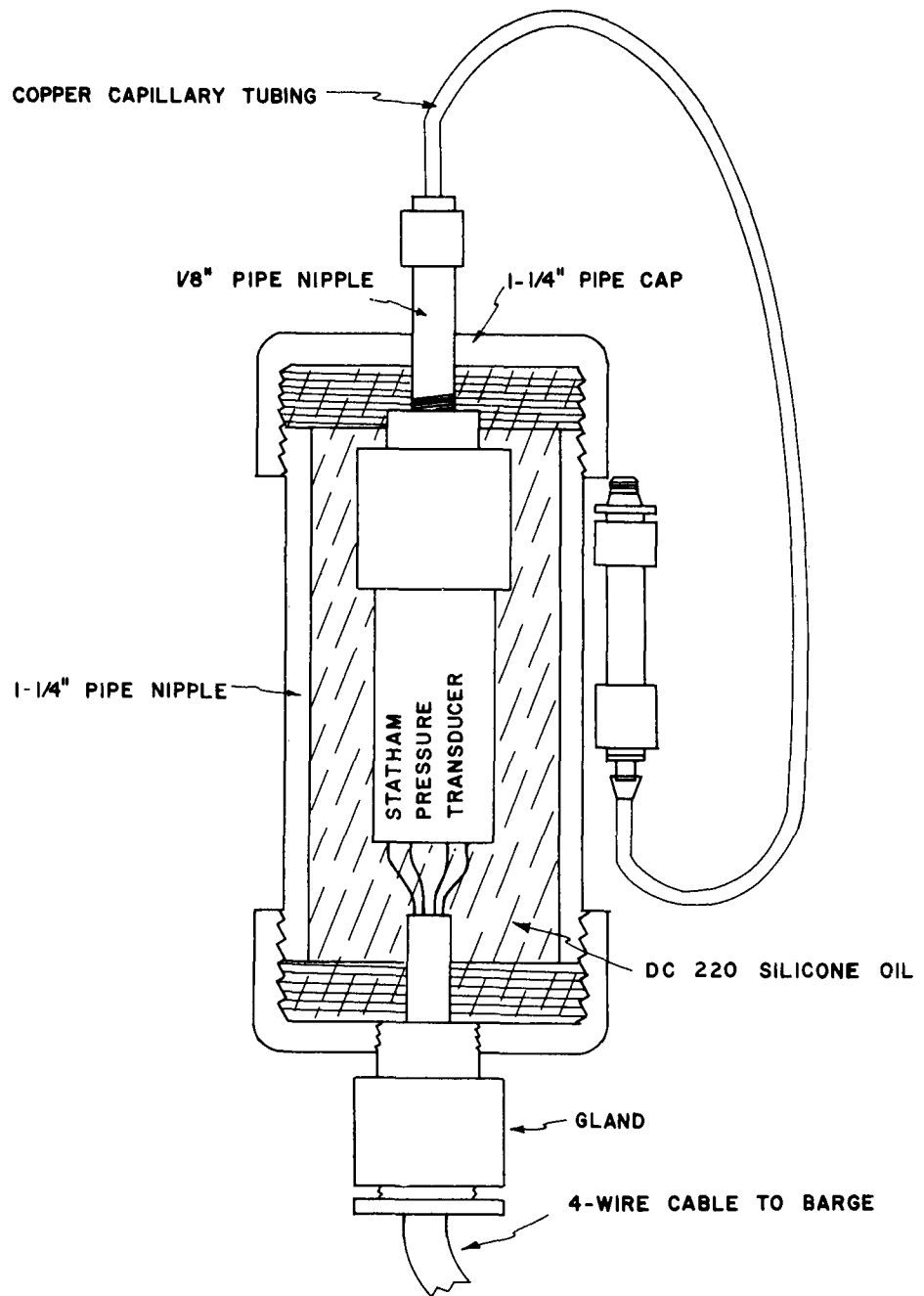


Figure 2.6 Detail of pressure transducer and protective case. Capillary tubing protected transducer bellows from initial peak explosion shock pressure.

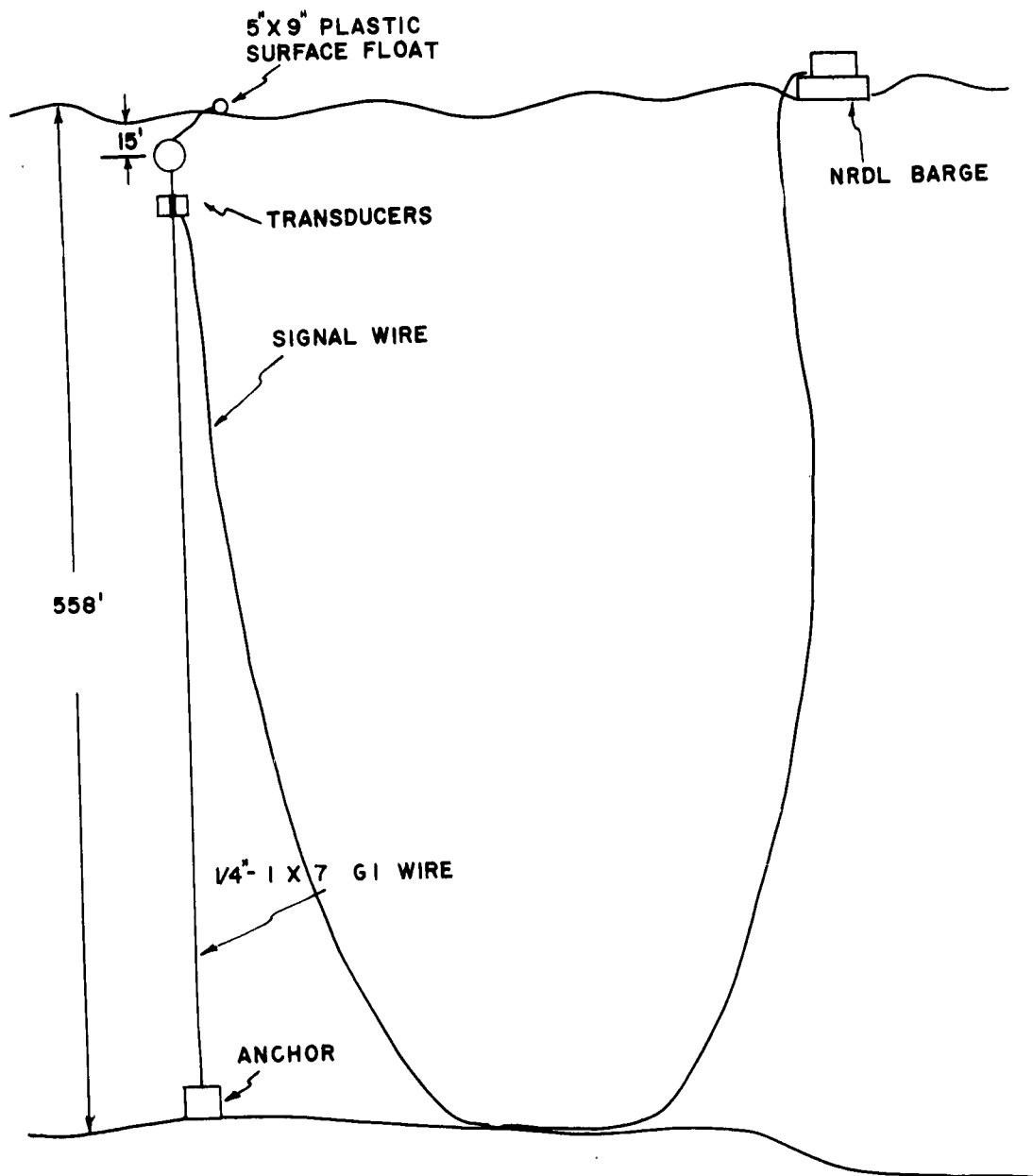


Figure 2.7 Transducer installation at Station A.

AC signals were amplified, demodulated, and recorded on an oscillograph aboard the USNRDL Barge. The barge also was evacuated during the actual shots so the system was programmed to operate autonomously after a start signal from the NRDL Master Controller. Circuit details are shown in Figure 2.8.

Fiduciary zero was established by the arrival of the shock wave at the transducers, and subsequent time-control was established thru a one-half second time hack, recorded on the oscillogram, generated by a Ulysse-Nardin chronometer.

The depth of transducer installation and a slightly non-linear output from the amplifiers required that the raw data be corrected to calibration curves and to known depth attenuation factors. Overall resolution was of the same order as the photographic data.

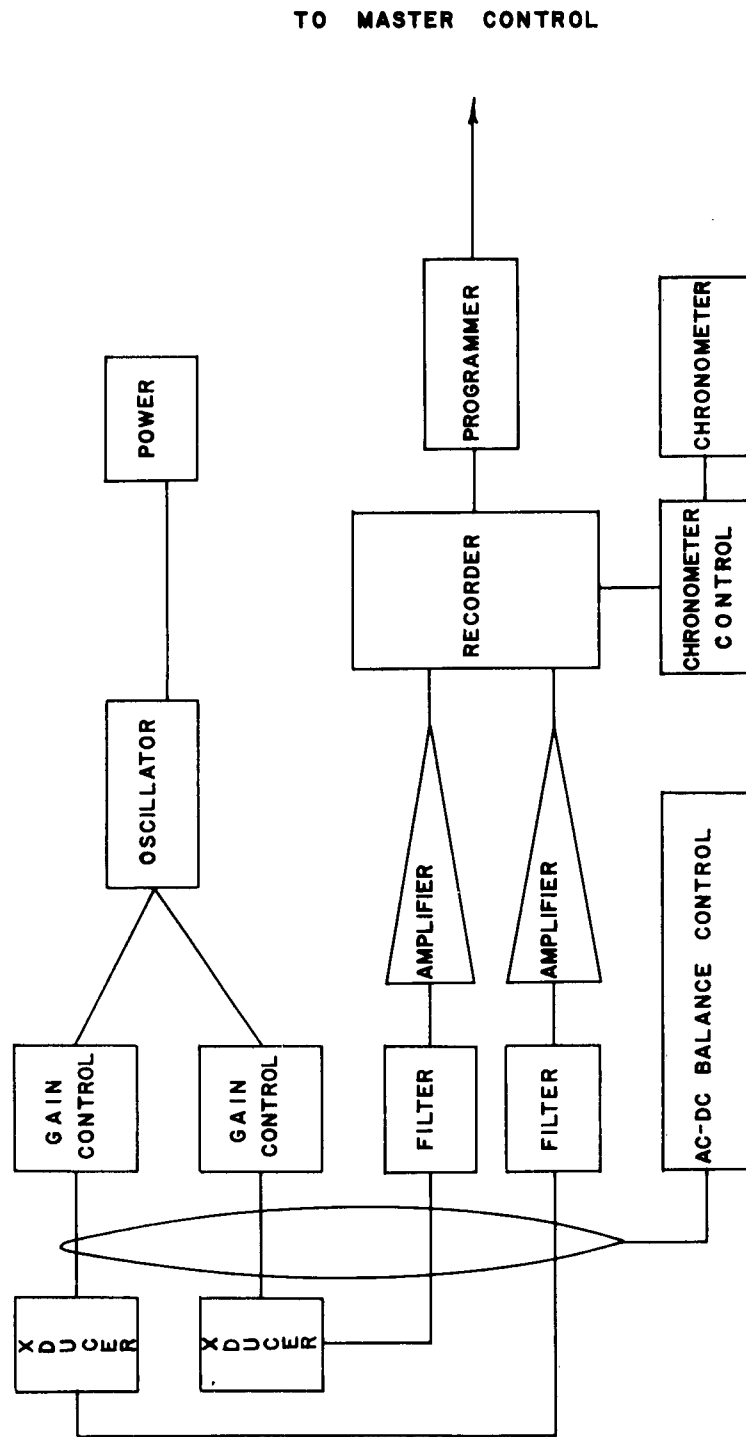


Figure 2.8 Block diagram of transducer electronics.

CHAPTER 3

RESULTS OF THE WAVE MEASUREMENTS

3.1 SHOT PARTICIPATION

Data pertaining to the various events and shot participation are listed in Table 3.1. Wave records were obtained at one or more stations for eight out of thirteen events, although simultaneous records were obtained at all three stations only for Shots 8 and 11. Even so, as will be shown, a single record suffices to tell the whole story of the wave history, and the spectrum of charge depths covered by the eight shots monitored essentially spans the entire region of interest from the standpoint of wave generation, with the exception of zero charge depth, for which no shot was scheduled.

3.2 WAVE RESULTS

Wave measurements obtained at Stations A, B, and C are plotted in Figures 3.1 to 3.4, respectively. For Stations B and C the plots consist of surface elevations read directly from the camera films, with no corrections involved. The reading accuracy was ± 0.05 ft in both cases, although occasional gaps in the early records at Station B occurred when the spar at Station C momentarily obscured the more distant spar. This situation was later

TABLE 3.1 SHOT PARTICIPATION AND GEOMETRY

ND, no data obtained; NI, instrumentation not yet installed

Shot	Date	Charge Depth	Range to Surface		Remarks
			Station A h = 558 ft	Station B h = 205 ft	
		feet	feet	feet	
4	Aug 5	6.6	NI	1524	NI
5	Aug 9		NI	ND	ND
6	Aug 23		NI	ND	ND
7	Aug 26	140.0	NI	1540	2230
8	Aug 30	80.0	940	1552	2240
9	Sept 2	35.0	ND	1564	2252
10	Sept 13	7.5	946	ND	ND
11	Sept 19	15.6	932	1568	2254
12	Sept 26	15.4	944	ND	ND
13	Oct 2	17.0	948	ND	ND

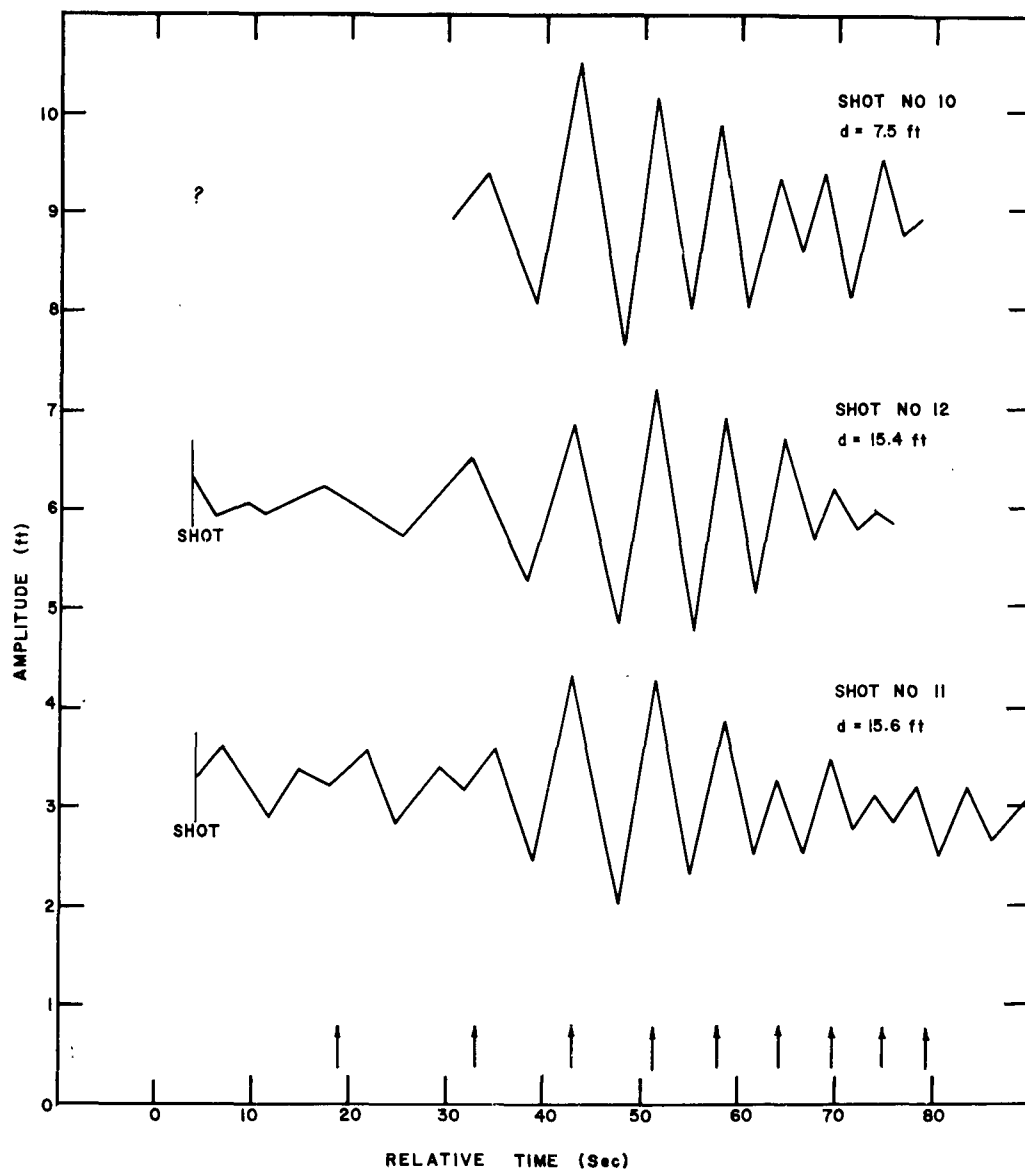


Figure 3.1 Wave records from Station A (30 psi transducer)

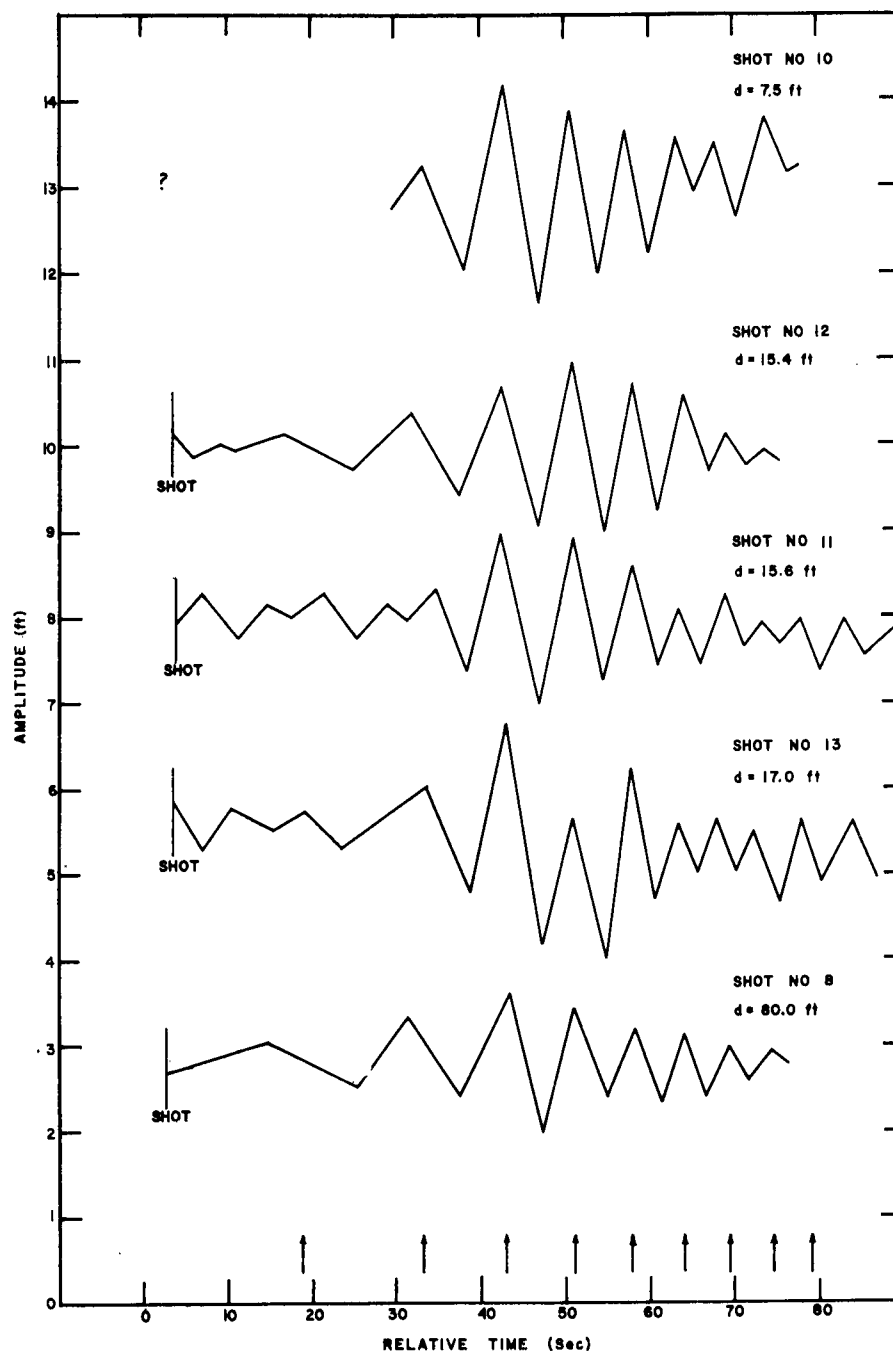


Figure 3.2 Wave records from Station A (40 psi transducer).

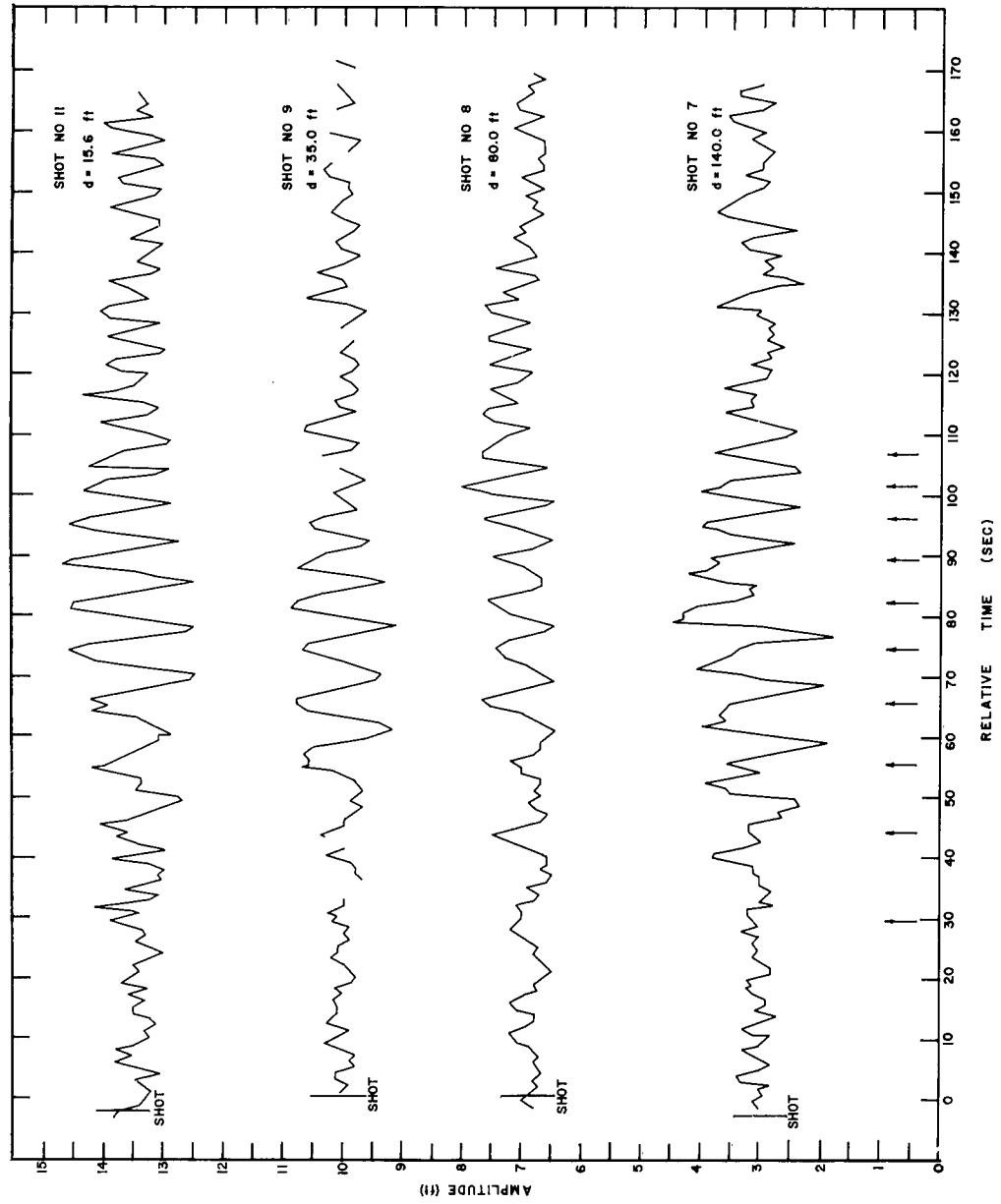


Figure 3.3 Wave records from Station B.

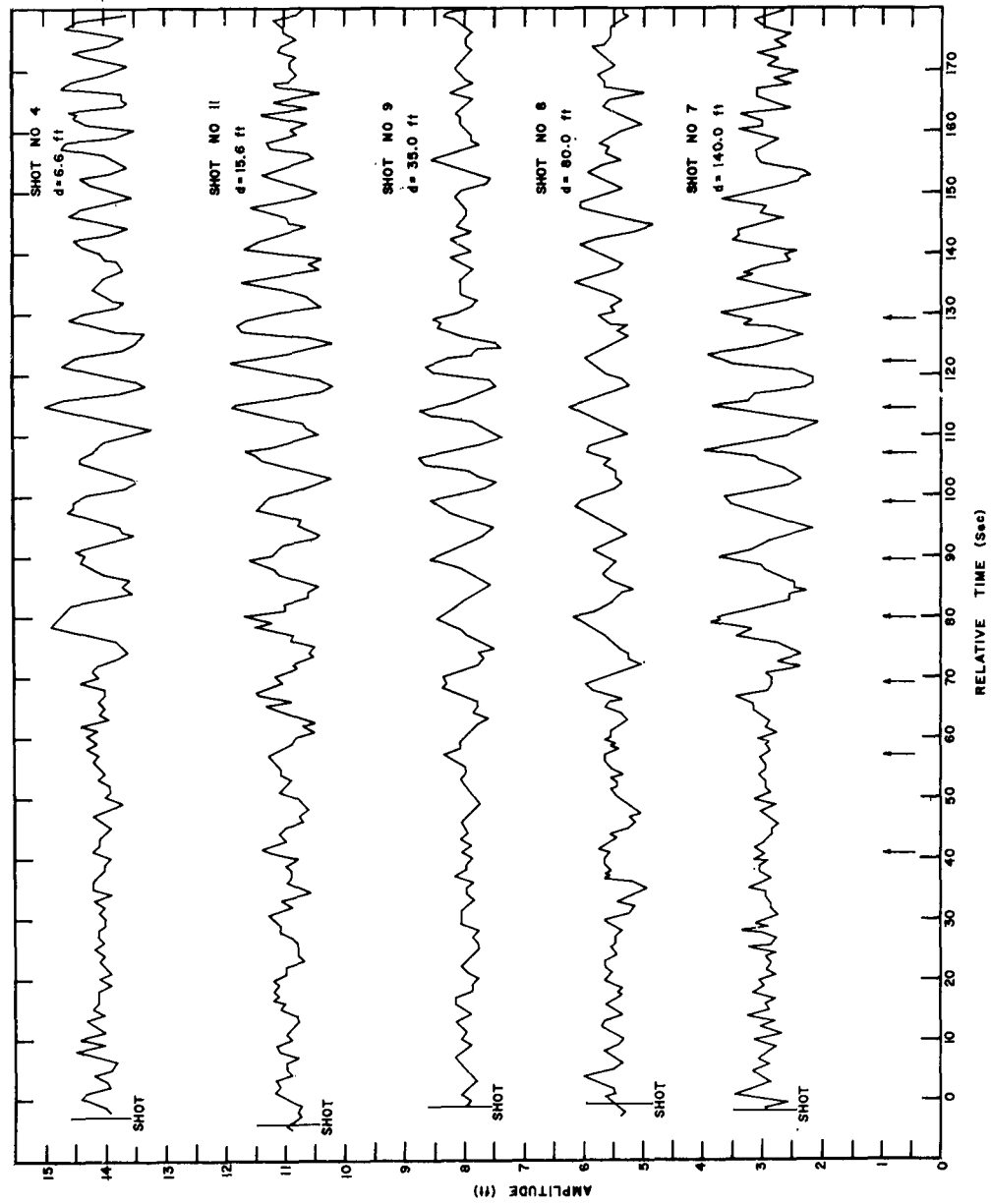


Figure 3.4 Wave records from Station C.

corrected by shifting the camera location slightly.

Figures 3.1 and 3.2 are plots of the crests and troughs of the oscillograms recorded at Station A for the 30 and 40 psia transducers, since the original records were too long to be reproduced directly. These data, together with their respective arrival times provide sufficient information for wave analysis. The amplitude data were multiplied by a calibration factor obtained from the amplitude of a known electrical step-signal applied to each oscillogram before and after each shot. Since the transducers were submerged beneath the surface, it was necessary in the later analysis of these data to apply an orbital-pressure correction which depended upon wave frequency and also upon the local tide height relative to the known tide height at the time of transducer installation, as described in Section 4.3 below.

Following Shot 10 the wave amplitudes at Station A computed for the 30 psi transducer differed from those for the 40 psi transducer by a constant factor of 1.25. This discrepancy is believed to be due to inadvertent cross-connection of the transducer cables to their respective calibration and balance networks. The logarithmic mean of the two transducer amplitudes at a given frequency was taken as the most appropriate value

of the real amplitude, and was found to give results consistent with those at the two spar stations, B and C.

Comparison of the wave records obtained in different depths of water reveals the profound effect of depth in governing the history of the wave train, and shows immediately that the results of tests having differing geometries and yields cannot be compared without consideration of the local water depth. Shot 11 was observed at all three stations at a time of exceptionally low background, and thus affords the best standard for comparison. At Station A ($h = 558$ ft, $r = 950$ ft) the wave train is still quite compressed and the second or third wave is the highest. At Station C ($h = 28$ ft, $r = 2250$ ft) the train is greatly expanded in time and the 11th wave is the highest. The effect of shoaling water is also reflected in the amplitude of the highest wave, which is about 30% higher than it would have been in water of constant depth ($h = 300$ ft) equal to that at the shot site.

CHAPTER 4

ANALYSIS OF RESULTS

4.1 PURPOSE OF THE ANALYSIS

In order to compare these results with those from other experiments, and to test the theoretical predictions for impulsively generated waves in water of uniform depth, it is first necessary to reconstruct from these data the wave trains which would have been produced from the same shots in water of uniform depth, $h = 300$ ft, the depth at Surface Zero. The procedure consists of two steps. First, the wave arrival times must be calculated for the existing stations as a check on the method, and also for some given range in uniform depth. The phase travel-times are virtually independent of the nature of the source, and hence are only slightly affected by the depth of burst or the shot yield. Second, the amplitude of the wave envelope as a function of frequency must be calculated in order to determine which waves of the reconstructed train will be highest, and also in order to later deduce the nature of the equivalent source. The amplitude spectrum of a wave train is independent of the phases and can be computed separately. Interest in the phases principally stems from the desirability of predicting which waves of the

reconstructed train will be highest, and when they will have passed.

The procedure followed in making the above calculations is the application of geometric optics in a linear continuum, and is set down here in some detail, since it seems not to have been previously attempted in problems of this nature. The reason for this omission is probably that solutions to the equations describing the field of motion for arbitrary topography cannot be obtained in closed form, but must be found by numerical approximation. In particular, these equations are functions of the local water depth h and wave number k , which are related to the wave frequency ω by the Hamiltonian equation

$$\omega^2 = gk \tanh kh \quad (1)$$

(g = gravity) which must be solved for k wherever the motion is to be specified. In a two-dimensional cartesian system two orthogonal components of the wave number will ordinarily have to be considered. This difficulty will be avoided here by selecting a propagation path such that the normal coordinate everywhere vanishes; i.e. along that ray which coincides with the least-time path.

4.2 CALCULATION OF THE PHASE ARRIVALS

In water of uniform depth h the phases θ of a dispersive wave system will propagate along curves in the space-time plane which are solutions of the differential equation $dr/dt = c(k)$, where c is the local phase velocity and r and t are the space and time coordinates. These solutions have the form $\theta(r,t) = \text{constant}$. In the case of a centered (radially symmetric) system resulting from an initial deformation of the water surface given by $y = y_0 f(r)$, $t = 0$, these solutions become (Ref 2)

$$\cos(\omega t - kr) = m = \text{constant} \quad (2)$$

If attention be focused on, say, the positive maxima (crests) of the system observed to be passing a station at a distance $r = r'$ from the origin, then $m = 1$, and the times of arrival of successive crests in their order n of occurrence will be

$$t_n = \frac{2\pi(n-1) + k_n r'}{\omega_n}, \quad n = 1, 2, \dots \quad (3)$$

where now k_n and ω_n are the local values of the wave number and frequency of the n th crest at time t_n .

But $t_n = r'/V(k_n)$ is also the time of arrival of k_n propagating at constant group velocity

$$V_n = V(k_n, h) = \frac{1}{2} \left[\frac{g}{k_n} \tanh k_n h \right]^{\frac{1}{2}} \left[1 + \frac{2k_n h}{\sinh 2k_n h} \right] \quad (4)$$

over the distance r' . Thus the solution of (3) for a given n is obtained by finding that value of k_n which satisfies the identity

$$\frac{2\pi(n-1) + k_n r'}{\omega_n} = \frac{r'}{V_n} \quad (5)$$

The above reasoning can be generalized to compute phase arrival times in water of variable depth along a ray path s by summing the increments Δt_n required for the phases to propagate in depths $h(s)$ assumed constant over the small path increments Δs which suitably approximate the bottom profile.

Before applying this procedure to the wave systems considered here, the conditions required for the applicability of linear theory and geometric optics were examined; namely, that, if $\eta[\omega(k, h)]$ is the wave amplitude

$$\eta k / (kh)^3 \ll 1 \quad (6.a)$$

$$kh \gg dh/ds \quad (6.b)$$

at all frequencies considered. The limiting situation arises in both cases when η is large and k and h are small; i.e., near the front of the wave train at the shallowest station. From the record of Shot 11 at Station C the time interval between the first two crests is about 13 sec and $\eta \div 0.25$ ft. From (1) $kh \div .22$, and (6.a) is satisfied. But the bottom slope $dh/ds \div 0.1$ and thus the wave amplitudes computed in the next section may be somewhat in error at low frequencies. As will be shown, however, the higher waves at this station are associated with a value of $kh = 0(1.0)$ and the method should apply without reservation.

The theoretical arrival times for the first ten crests at all three stations were determined by dividing the bottom profiles into 50 ft increments of distance arranged in order of decreasing depth,¹ and programming equation (5) on the University of California's CDC 1604 computer at La Jolla. For these calculations the slight changes of shot position were ignored and the distances

¹ The sum is independent of the order of summation, and the trial and error solution converges rapidly if the 1st trial in each case was that value of k_n determined for the preceding increment.

to Stations A, B, and C were taken as 950, 1550, and 2250 ft, respectively. The path chosen was the direct route in all three cases, which coincided very nearly with the slope gradient for Stations A and B. The direct route to Station C deviated about 30° from the slope gradient, but the water depth was everywhere great enough so that the least-time path can be shown to differ insignificantly from this route for any frequency considered here. Figures 3.1 to 3.4 also show the computed crest arrivals (small arrows), which can be seen to agree with those observed quite closely. The trains are plotted in order of increasing charge depth with the prominent phases aligned in time, because the theoretical premise of an instantaneous initial surface deformation ignores the finite and slightly variable time-dependence of crater formation upon charge depth. The fiduciary zero-times shown in these figures indicate a slight progressive phase lag with increasing charge depth. It is concluded that the linear theory adequately predicts phase arrivals in water of variable depth.

4.3 WAVE AMPLITUDE CHANGES IN WATER OF VARIABLE DEPTH

Within the regime where the laws of geometric optics apply and where the phase speed is not a function of amplitude, energy is considered to be conserved between

adjacent rays and also between adjacent frequencies. That is to say, if one forgets the phases altogether, and considers the field of wave energy to be defined as a continuum of "patches," any such patch being bounded in the direction of propagation by adjacent frequencies and parallel to this direction by adjacent rays, then as this patch propagates through the continuum at its characteristic group velocity, the local wave amplitude will vary as the square-root of the energy; i.e., inversely as the square-root of the patch area. In the special case where the field of motion is centered and where the origin of the ray path s coincides with the center of the disturbance, conservation of energy in a wave patch characterized by frequency ω is given by the expression²

$$E(\omega)/\pi\rho g = \eta_1^2 Z_1^2 \equiv \eta_1^2 \left[k_0(\omega) \int_0^{s_1} ds/k(s, \omega) \right] \left[-V_1(\omega) \int_0^{s_1} \partial/\partial k(1/2V^2) ds \right] = \text{const.} \quad (7)$$

where, in addition to symbols already defined, $E(\omega)$ = energy per unit frequency, ρ = density and the subscripts 0 and 1 refer to the origin and any point of observation

² A derivation of this relation is given in Appendix A.

respectively. In the case of an explosion, of course, the wave amplitude spectrum is unknown at the origin, but it is known in principle at all observation stations, and hence the applicability of theory to the present situation can be tested by evaluating the intensity factor Z at each station for a number of frequencies, and then comparing the product $(\eta Z)_\omega$ at a given frequency between stations.

This somewhat elaborate computational procedure was accomplished in the following manner. First, as in Section 4.2, the direct routes to all three stations were divided into n small, equal (50-ft) intervals Δs and the mean depth $h(s)$ tabulated for each interval. Equation (7) was then rewritten as

$$Z^2(\omega) = k_0 V_1 \Delta s^2 \sum_{0}^n (1/k) \sum_{0}^n \beta \quad (8)$$

where

$$\beta = - \partial / \partial k (1/2V^2) =$$

$$(8/g \tanh kh) \left[\frac{\frac{1}{4} - kh/\sinh 2kh - k^2 h^2 (1 - 2 \cosh 2kh) / \sinh^2 2kh}{(1 + 2kh/\sinh 2kh)^3} \right]$$

and, again, $k(\omega)$ is computed by trial-and-error from equation (1).

The envelope amplitudes $\eta(\omega)$ were obtained from the observed wave trains $\eta(t)$ at the three stations as follows. Any frequency ω propagates in water of depth h at group velocity

$$V = \partial\omega/\partial k = \partial/\partial k (gk \tanh kh)^{\frac{1}{2}} \quad (10)$$

and therefore, the time required for a given frequency to propagate to a point at a distance s_1 from the origin in water of variable depth $h(s)$ will be

$$t = \int_0^{s_1} ds/V \doteq 2\Delta s \sum_0^n \left[\left(\frac{g}{k} \tanh kh \right)^{\frac{1}{2}} \left(1 + \frac{2kh}{\sinh 2kh} \right) \right]^{-1} \quad (11)$$

where the $h = h(s)$ are the same depths previously tabulated. Smooth envelopes were drawn around the wave records $\eta(t)$ for Shot 11, from which the amplitudes were scaled directly at times determined from (11) corresponding to twelve selected frequencies spanning the appropriate time domain in frequency-wave number space. These spectral amplitudes have no permanent relation to the actual waves within the envelope, but each represents the amplitude any wave would have if

it arrived at the recording station at the same times at which the twelve frequencies arrived. This statement obtains because frequencies and individual waves propagate at different speeds and, in general, by different paths.

The spectral amplitudes $\eta(\omega)$ at Station A were then corrected for orbital-pressure attenuation by the factor $\left[\cosh k(z+h) / \cosh kh \right]$ where z is the transducer depth at the local tide stage and k is the wave number corresponding to each frequency. The corresponding values of $Z(\omega)$ were then computed from (8).

Table 4.1 lists the frequencies, arrival times, amplitudes, Z -values, and the products ηZ for all three stations. If the influence of variable water depth has been correctly taken into account in this analysis, the ηZ values should agree between stations at any particular frequency. Considering the marked fluctuations in the amplitudes of individual waves and the difficulty of drawing the most representative smooth curve through their extrema, the ηZ values agree fairly well over most of the frequency range; there appears to be a general tendency, particularly at mid-frequencies, for the values to be highest in shallow water and lowest in deep water. This effect is probably due to reflections from the shoreline, which are ignored in the analysis.

TABLE 4.1 SPECTRAL AMPLITUDES AND ENERGY DENSITIES
AT TWELVE FREQUENCIES FOR THREE OBSERVATION STATIONS

Data are from Shot 11.

Frequency	Station	Arrival Time	Spectral Amplitude	Intensity Factor	Spectral Energy Density
$\omega(\text{sec})^{-1}$		t(sec)	$2\eta(\omega)$ ft	$Z(\omega)\times 10^{-3}$	$2\eta Z\times 10^{-3}$
.183	A	9.9	0.20	1.67	0.35
	B	19.6	0.20	1.79	0.35
	C	32.3	0.25	1.51	0.35
.343	A	14.7	0.65	1.88	1.20
	B	27.8	0.45	2.54	1.15
	C	41.3	0.50	2.38	1.20
.433	A	24.3	0.80	1.66	1.30
	B	36.4	0.55	2.71	1.50
	C	50.5	0.60	2.84	1.70
.507	A	28.7	1.20	1.45	1.75
	B	45.0	0.70	2.75	1.90
	C	60.5	0.65	3.04	1.95
.585	A	35.0	2.05	1.28	2.60
	B	54.8	1.10	2.32	2.55
	C	73.5	0.80	3.03	2.40
.673	A	35.6	2.60	1.18	3.05
	B	64.8	1.40	2.00	2.80
	C	88.7	1.00	2.90	2.90
.765	A	43.9	3.00	1.09	3.30
	B	74.2	1.80	1.70	3.20
	C	105.0	1.20	2.73	3.25
.863	A	48.4	3.25	1.03	3.35
	B	83.8	1.95	1.67	3.25
	C	119.5	1.50	2.64	3.95
.956	A	54.9	2.85	0.97	2.75
	B	93.0	1.85	1.58	2.90
	C	133.5	1.35	2.53	3.40
1.050	A	60.3	2.30	0.93	2.15
	B	102.5	1.45	1.52	2.20
	C	147.0	1.00	2.42	2.40
1.143	A	65.8	1.60	0.89	1.45
	B	111.0	0.95	1.45	1.40
	C	160.0	0.60	2.32	1.40
1.240	A	71.2	0.00	0.86	0.00
	B	120.5	0.00	1.39	0.00
	C	173.0	0.00	2.21	0.00

Some recent unpublished qualitative observations by the authors in connection with wave tank experiments support this view. Monochromatic wave trains directed against beach slopes typical of the HYDRA environment indicate that reflections manifest themselves as an increase in the wave amplitude observed offshore, but without change of phase. The observed enhancement appeared to be somewhat frequency sensitive and was of the order of 30% in some cases. In the present situation the wave trains were both centered and dispersive, and thus any influence of reflection would be most important at the station nearest the shore, and die out rapidly in deeper water. Pending more precise results, then, the tentative conclusion is that the application of geometric optics to shoaling water waves is also confirmed.

4.4 RECONSTRUCTION OF THE AMPLITUDE SPECTRUM OF THE WAVE TRAIN IN WATER OF CONSTANT DEPTH

The linear theory for waves produced by an explosion in water of finite depth (Ref 2) gives the phase and amplitude spectrum of the wave train as a function of time and distance, starting with the Hankel transform of the initial impulse or surface elevation at time zero. It is therefore necessary to reconstruct the amplitude

spectrum of the observed wave train as it would have been recorded at (any) range R in water of uniform depth in order to deduce the nature of the source. For uniform depth equation (8) becomes

$$Z_o^2(\omega) = V_o R^2 \beta_o \quad (12)$$

Taking the RMS value $(\Sigma \eta^2 Z^2 / 3)^{\frac{1}{2}}$ of the products ηZ listed in Table 4.1 at each frequency as that value least susceptible to random error, the spectral amplitudes will be given by

$$\eta(\omega)_R = (\Sigma \eta^2 Z^2 / 3)^{\frac{1}{2}} / Z_o \quad (13)$$

and the corresponding arrival times are obtained from (11) which, for constant depth, is

$$t(\omega) = R / V_o(\omega) \quad (14)$$

Table 4.2 gives numerical results for the case $h = 300$ ft, $R = 1000$ ft and the reconstructed envelope of the wave train for Shot 11 is shown in Figure 4.1. The wave train in this figure circumscribed by the envelope was calculated from the theory, as described below.

TABLE 4.2 SPECTRAL AMPLITUDES AT TWELVE FREQUENCIES
FOR SHOT 11 CORRECTED TO UNIFORM WATER DEPTH $h = 300$ ft
AT RANGE $R = 1000$ ft.

Frequency	Arrival Time	Spectral Amplitude		
$\omega(\text{sec})^{-1}$	$t(\text{sec})$	$(\Sigma \eta^2 Z^2 / 3)^{\frac{1}{2}}$ $\times 10^{-3}$	Z_0 $\times 10^{-3}$	$\eta(\omega)$ ft
.183	11.9	0.35	1.35	0.13
.343	17.8	1.18	1.79	0.33
.433	23.9	1.51	1.93	0.39
.507	29.8	1.87	1.64	0.57
.585	35.6	2.52	1.42	0.89
.673	41.8	2.92	1.25	1.17
.765	47.6	3.25	1.15	1.41
.863	53.6	3.43	1.08	1.61
.956	59.6	3.03	1.03	1.47
1.050	65.3	2.25	0.98	1.15
1.143	71.3	1.42	0.94	0.75
1.240	77.2	0.00	0.90	0.00

TABLE 4.3 MAXIMUM SPECTRAL AMPLITUDE AT VARIOUS
CHARGE DEPTHS

Shot	Station	Maximum Amplitude	Charge Depth
		$\eta''(\text{ft})$	$d(\text{ft})$
10	A	1.60	7.5
12	A	1.45	15.4
11	A	1.55	15.6
	B	1.50	
	C	1.80	
13	A	1.45	17.0
9	B	1.25	35.0
	C	1.60	
8	A	1.35	80.0
	B	0.95	
	C	1.20	
7	B	1.65	140.0
	C	1.95	

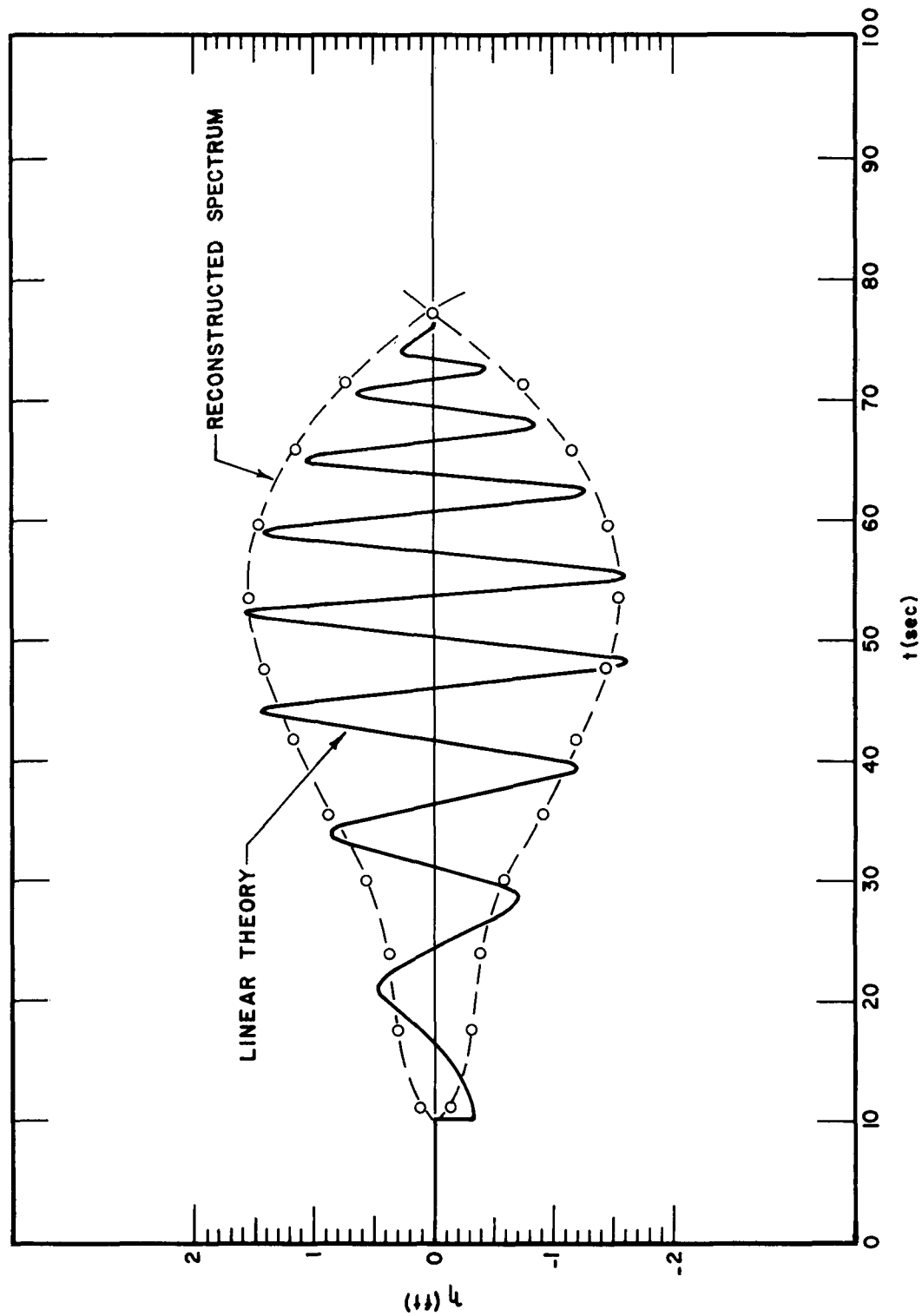


Figure 4.1 Reconstructed wave envelope for Shot 11 at range $R = 1000$ ft in water depth $h = 300$ ft. Wave train within envelope was computed from theory.

4.5 THE EQUIVALENT SOURCE

Although it is in principle possible to reconstruct a model for an equivalent source from the wave amplitude spectrum observed at a distance in water of uniform depth (Ref 3), the inherent nature of the solution requires an extremely well-dispersed spectrum--i.e., a very remote source, where the spectral amplitude changes only slightly over one wavelength. Moreover, the distribution of source strength with radius is extremely sensitive to the higher derivatives of the spectrum, such that this method is alone proscribed by the very approximate nature by which the spectrum for uniform depth was derived. It appears simpler and more accurate in the present case to make a guess as to the nature of the source from the general appearance of reconstructed spectrum, compute the spectrum predicted by theory, and make small adjustments until satisfactory agreement is obtained with the reconstructed spectrum.

The node in the reconstructed spectrum at about $t = 77$ seconds suggests that such a spectrum would be predicted by an initial parabolic crater in the water, since it is known that such craters are produced by explosions on land over a considerable range of charge submergence. For the case of an initial parabolic

depression of the form $y = y_0[1-(r/r_0)^2]$, where y_0 and r_0 are the depth and radius of the depression, respectively, the linear theory of Kranzer and Keller (Ref 2) predicts a wave train having an amplitude-time history at a distance r in water of depth h described by

(15)

$$\eta(t) = (2y_0/rk^2h) \left[\frac{kV(k)}{-dV/dk} \right]^{\frac{1}{2}} J_2(r_0k) \cos \left[kr \left(\frac{2}{1+2kh/\sinh 2kh} - 1 \right) \right]$$

This solution was normalized to the reconstructed train as follows. Let $t_0 = \sqrt{gh}$ and t' be the respective times of arrival of the front and first node of the envelope of the wave train. Then the wave number k' propagating with group-velocity V' which arrives at station r at time t' will be the root of the relation

$$V' = t_0/t' = \frac{1}{2} \left(\frac{g}{k'}, \tanh k'h \right)^{\frac{1}{2}} \left[1 + \frac{2k'h}{\sinh 2k'h} \right] \quad (16)$$

Since the first node corresponds to the first zero of the Bessel function $J_2(r_0k')$, which occurs when its argument has the value 5.14, the radius of the depression is determined as $r_0 = 5.14/k'$. In the present case the appropriate values are (for $t' = 77$ sec)

$k' = 0.048$, $r_0 = 108$ ft, which is in good agreement with the radius of the explosion plume determined independently from photographic data. Having determined r_0 equation (15) was programmed on the computer and the value of $y_0 = 29.5$ ft was found, after a trial or two, to give the best fit to the reconstructed wave train. Both the reconstructed envelope and computed wave systems are shown in Figure 4.1. The amplitude agreement is in general satisfactory, although the theory predicts a small negative bore at the front of the disturbance, due to a net removal of water by the explosion. By analogy to craters on land, however, it is known that the material thrown out of the crater rapidly descends forming a raised lip around the crater zone. A more accurate initial model taking this phenomenon into account would not show a bore.

4.6 THE EFFECT OF VARIABLE CHARGE DEPTH

Comparison of the wave trains from different shots recorded at the same station reveals a significant change in the amplitudes of the highest waves with varying charge depth, but little change in the arrival time of the amplitude maximum. The theoretical inference of this observation is that the vertical scale of the source disturbance is much more sensitive to the vertical

position of the charge than the horizontal scale. Thus the effect of varying the charge depth can be examined by comparing the spectrum amplitudes at a single frequency, because the vertical scale of the source affects all frequencies similarly, while its horizontal extent determines the energy distribution among frequencies.

Taking $\omega'' = gk'' \tanh k''h = 0.88 \text{ sec}^{-1}$ for Shot 11 as that frequency typical of the amplitude maxima of all wave trains at any station, the corresponding spectral amplitudes $\eta(\omega'')$ were read from smooth envelopes drawn around the wave trains. These amplitudes were then multiplied by their appropriate intensity ratios $Z(\omega'')/Z_0(\omega'')$ to convert them to equivalent amplitudes in uniform depth $h = 300 \text{ ft}$. The resulting spectral amplitude maxima with their respective charge depths are given in Table 4.3. In general it can be said that the effect of increasing charge depth is to reduce the maximum wave amplitude in a somewhat irregular fashion, although the amplitude obtained for the deepest shot ($d = 140 \text{ ft}$) appears to be anomalously high. The total range of amplitude is smaller than a factor of two. That these results are consistent with those from other tests with different charge weights and water depths will be shown in the following section.

CHAPTER 5

COMPARISON WITH OTHER TESTS

5.1 THE SCALING LAW FOR VARIABLE CHARGE WEIGHT

Equation (15) gives the wave amplitude as a function of time at a given distance in terms of initial depth y_0 and radius r_0 of a parabolic crater. It is known empirically that the dimensions of craters produced in solid materials by charges of different weights scale approximately as fractional powers of the charge weight, provided that the charge depth is similarly scaled. If it is assumed that craters in water should obey the same scaling laws, and if attention is focused on the amplitude spectrum of the wave train, (15) can be generalized to include the effect of variable charge weight W and (uniform) water depth h . Ignoring the phase factor, the spectral amplitudes will be given by

$$\eta[B k(B)]_r = \frac{2B^a y_0}{k^2 h} \left[\frac{kV(k)}{-dV/dk} \right]^{\frac{1}{2}} J_2(B^b r_0 k) \quad (17)$$

Where $B = W/W_0$ is the dimensionless charge weight in terms of a reference weight W_0 .

Since interest lies chiefly in the largest waves in the spectrum, equation (17) was programmed in the

computer and the spectral amplitude maximum $\eta''r$ and its corresponding wave number k'' determined as a function of B .³ It was found that over a very considerable range of B these relationships can be represented by the very simple expressions

$$\eta''r/B^{a+b} = M \quad (18a)$$

$$k''B^b = N \quad (18b)$$

where the constants M and N are empirically determined, and depend only on the reduced charge depth d/B^b .

5.2 DETERMINATION OF THE YIELD EXPONENTS

The availability of other experimental results on a much smaller scale permits comparison with these results and a test of the theoretical generalization given by (17). Reproductions of some 80 wave trains from TNT explosions of $\frac{1}{2}$, 2, and 10 lb charges at a variety of charge depths

³ The solution fails when B becomes so large (k'' so small) that $B^b r_0 \geq h$, because of certain approximations made in deriving the linear solution.

were obtained through the courtesy of the U. S. Army Corps of Engineers.⁴ All tests were conducted in water of uniform depth $h = 20$ ft, and the waves were recorded at several stations within the range $24 \text{ ft} < r < 86 \text{ ft}$. Smooth envelopes were drawn around these wave trains and the maximum amplitudes $\eta''(t)$ and their arrival times t'' read directly from the records. The dimensionless wave numbers k'' corresponding to the amplitude maxima were then determined by trial-and-error from the relation

$$t'' = r/V'' = 2r\left(\frac{g}{k''} \tanh k''h\right)^{-\frac{1}{2}} \left[1 + \frac{2k''h}{\sinh 2k''h}\right]^{-1} \quad (19)$$

which will be recognized as the equivalent of (11) for constant depth h . The form of equations (18) suggests that the scaling law given by (17) can be examined if M and N are plotted against $D = d^b$, the reduced charge depth. The resulting distribution of empirical data points are, hopefully, to be optimized into a continuous curve by a suitable choice of the exponents a and b .

⁴ Waterways Experiment Station (WES), Vicksburg, Mississippi.

Equation (18b) can be solved for b at once by plotting B against k'' for the charge depth $d = 0$.⁵ The logarithmic plot (Fig 5.1) yields $b = 0.3$, which is also a typical value for scaling crater radii from explosions in soft soil (Ref 4). The same figure also shows $\eta''r$ plotted against B from which the line giving the least-squares fit has a slope at $b = 0.54$, hence, $a = 0.24$ for this charge depth. Again, this value is consistent with the crater depth scaling exponents empirically derived from explosions in soils and sand.

5.3 COMPARISON OF THE NORMALIZED RESULTS

Table 5.1 lists all HYDRA and WES data considered here, together with the corresponding values of M and N (equation 18) and D , computed using the above determined exponents. Figure 5.2 is a semilogarithmic plot of M against D . The dashed line in the figure was drawn by inspection because the interpretation of the data distribution is somewhat subjective. The general shape of the curve, if accepted, implies that the mechanism

⁵ There was no HYDRA test with $d = 0$, but it has already been noted that k'' changed only slightly with charge depth in these experiments, and the shallowest shot (Shot 4) was at $d = 6.6$ ft, or very near the surface on a reduced depth basis.

TABLE 5.1 MAXIMUM SPECTRAL AMPLITUDE M AND ASSOCIATED
WAVE NUMBER N AS A FUNCTION OF REDUCED CHARGE DEPTH D

Shot	Station	Reduced Charge Weight $B=W/W_0$	$M=\eta''r/B^{0.54}$	$N=k''B^{0.3}$	$D=d/B^{0.3}$
<hr/>					
$W_0 = 1 \text{ lb}$					
HYDRA II-A ($h_0 = 300 \text{ ft}$)					
7	B	14,450	9.3	0.35	7.9
	C		11.1	0.37	
8	A		7.6	0.38	4.5
	B		5.5	0.35	
	C		6.9		
9	B		7.1	0.32	2.0
	C		9.0	0.35	
10	A		9.1		0.4
11	A		8.9	0.33	0.9
	B		8.5	0.42	
	C		10.4	0.37	
12	A		8.4	0.34	0.9
13	A		8.2		1.0
<hr/>					
WES ($h_0 = 20 \text{ ft}$)					
	Average				
C-3-5	6-9	10.0	6.6	0.45	0.0
C-4-4	6-9		8.6	0.42	0.05
C-9-3	6-9		7.0	0.41	1.1
C-10A-1	6-9		10.3	0.41	2.4
C- *	6-9		3.8	0.45	5.4
B-3-6	7-10	2.0	12.6	0.41	0.0
B-4-6	7-10		12.6	0.39	0.05
B-9C-3	7-10		7.0	0.34	1.8
B-14-5	7-10		8.3	0.34	3.8
A-3-6	7-10	0.5	7.6	0.41	0.0
A-4-9	7-10		9.1	0.39	0.05
A- *	7-10		8.8	0.37	2.2
A-10C-1	7-10		8.8	0.34	2.7
A-19-2	7-10		3.7	0.40	5.8

* Shot number not available

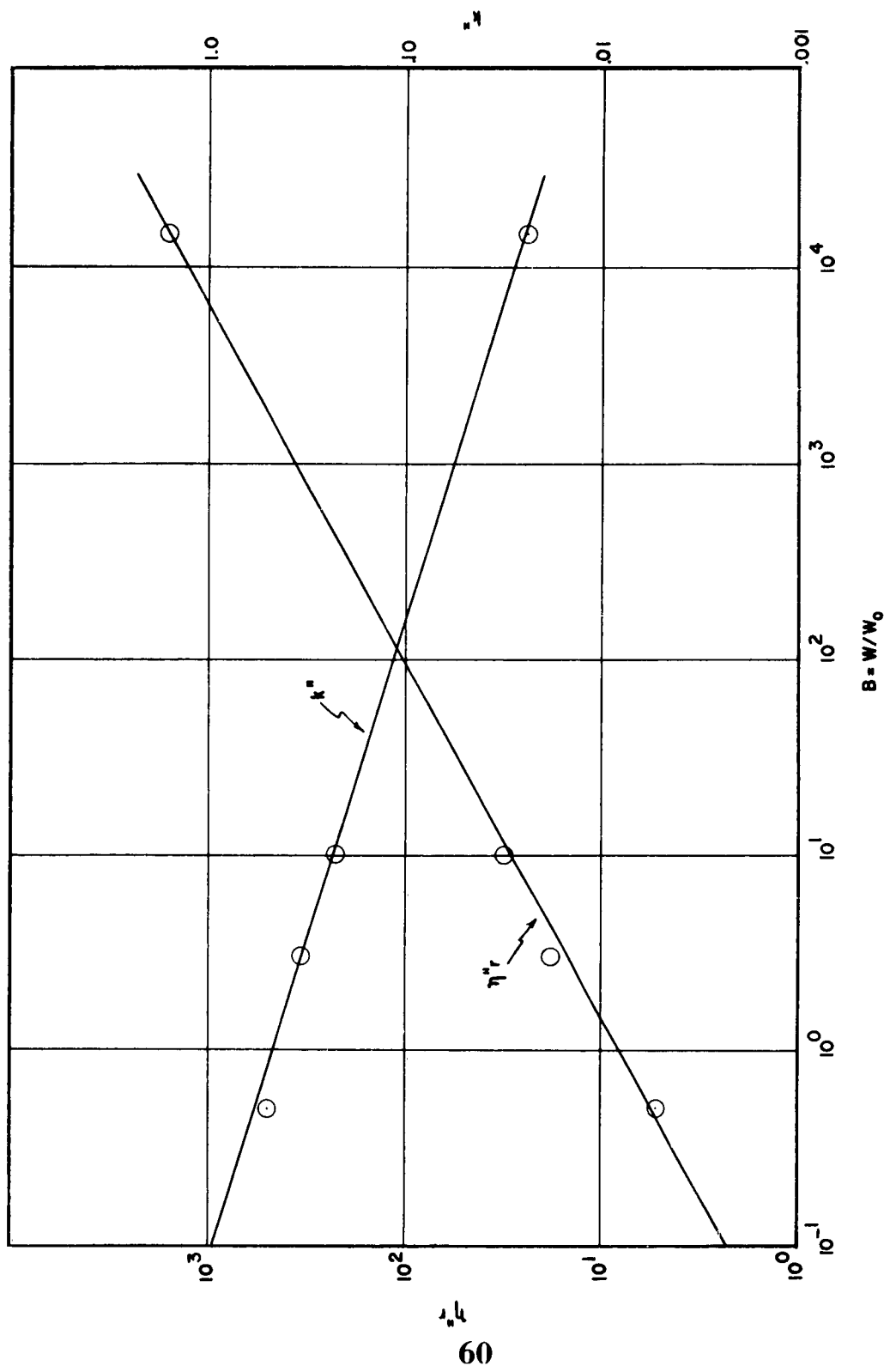


Figure 5.1 Wave number and amplitude times range at amplitude maximum versus charge weight, for zero charge depth.

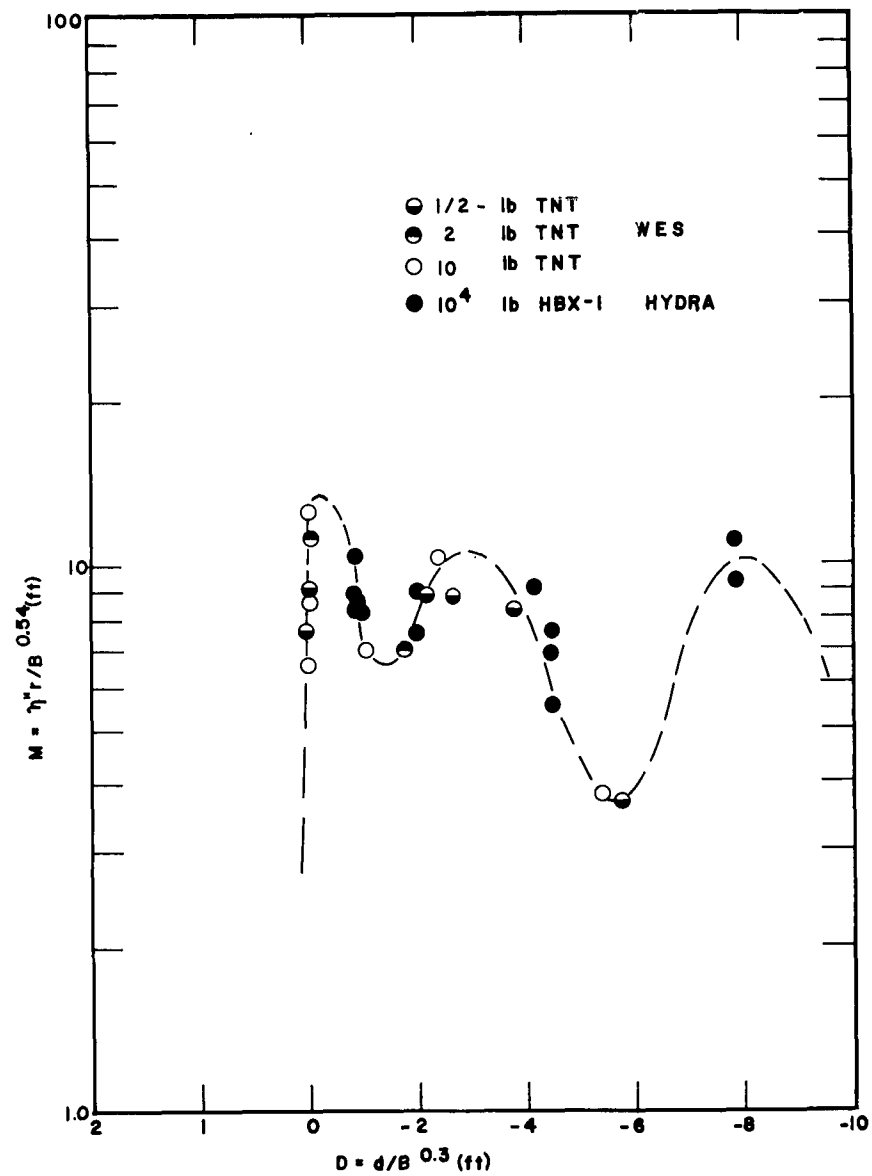


Figure 5.2 Variation of maximum wave amplitude with charge depth at constant charge weight and range.

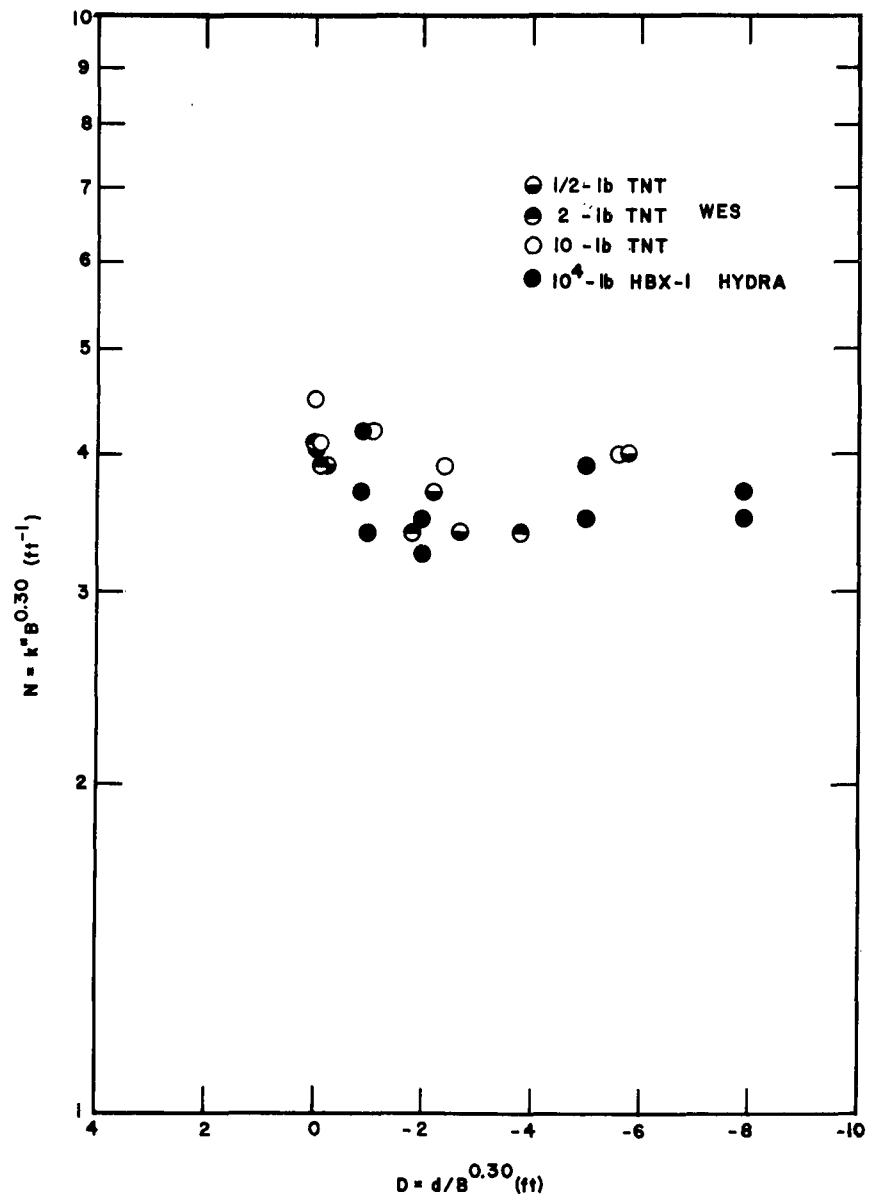


Figure 5.3 Wave number at amplitude maximum versus charge depth at constant charge weight.

of wave generation is quite complicated. The highest waves are evidently produced by shots at--or very near--the surface, and the rapid rise of the curve suggests that above-surface shots are only very weakly coupled to the water. As the charge depth increases the amplitude function appears to go through several successive minima and maxima, which may well be linked to the phase at which the explosion cavity or bubble enters the surface. The remarkable feature of this curve is that data from explosions differing by an order of magnitude in depth and four orders in yield agree within 10% when compared on the scaling basis derived above.

Figure 5.3 shows the wave number parameter N versus D . The data are less regularly disposed than those for amplitude, probably because the wave number is a rapidly changing quantity near the front of the train and is more difficult to determine precisely where the train is poorly resolved; i.e. where there are only a few waves within the first maximum of the amplitude envelope. In general, increasing charge depth slightly decreases the wave number at the wave amplitude maximum. Since the frequency ω associated with the wave number k is given by $\omega = \sqrt{gk \tanh kh}$ it is apparent that $\omega \sim \sqrt{k}$ for moderate or large relative water depth

($kh \geq 3$), and hence under these conditions $\omega'' \sim W^{0.15}$.
Thus ω'' is even less sensitive to yield than it is
to charge depth.

CHAPTER 6

DISCUSSION

6.1 LIMITATIONS OF THE LINEAR SOLUTION

The procedure followed in this analysis was to force a linear solution to a given set of experimental data and then to generalize it in terms of variable yield and water depth and to show that it adequately describes the results from other tests on a much smaller scale. Evidently, the solution in no way describes the hydrodynamic phenomena leading to the wave train, nor does it start with a realistic input--the normalized crater depth $y_0 = 29.5$ ft (Shot 11) is manifestly ridiculous for an explosion of 10,000 lbs of HBX-1 at 15.6 ft beneath the surface. The fact that the solution works so well is an expression of the fact that the important features of the early stages of the ensuing wave train are remarkably insensitive to the details of the source. That is to say, the train of waves produced by dropping a round ball or a square brick into water are virtually identical except for the energy at high frequencies, which controls the way the train dies away. Since the latter is relatively unimportant from the standpoint of wave effects, it can usually be ignored. The solution has been shown to agree with

observations within about 10% over an impressive range of charge weights, and it is doubtful that a complete understanding of the very complicated explosion hydrodynamics would substantially improve this capability. It clearly fails when the water is too shallow, or when the topography over which the waves system propagates is too irregular. Nevertheless it should prove of considerable utility as input for problems of wave runup and local effects where the restrictions are not violated.

6.2 WAVEMAKING EFFICIENCY

The linear solution for wave generation assumes that all the potential energy of the normalized crater is converted into wave motion. The potential energy of a crater given by $y = y_0[1-(r/r_0)^2]$ is easily shown to be $E_p = \pi \rho g y_0^2 r_0^2 / 6$. For the case of Shot 11 ($y_0 = 29.5$ ft, $r_0 = 108$ ft) $E_p = 3.4 \times 10^7$ ft-lbs $= 1.1 \times 10^7$ cal. Taking the available thermal energy of HBX-1 as 1445 cal/gram, the wavemaking efficiency of Shot 11 was about 1.7%. The highest value for M (Fig 5.2) is about 12% higher than that for Shot 11, and therefore the maximum efficiency over the range of charge depths considered here was about 2%. From equation (17) one

finds that the product $y_0^2 r_0^2$ scales as $B^{1.08}$, and hence it is inferred that the wavemaking efficiency increases slightly with charge weight.

6.3 THE INFLUENCE OF ATMOSPHERIC PRESSURE

Water waves in a real atmosphere are actually interfacial waves between two fluids: air and water. But the density ratio between these fluids is so large that the effect of atmospheric pressure can be shown to be completely negligible insofar as the hydrodynamics of oscillatory wave motion is concerned. Atmospheric pressure, however, has a pronounced effect on the radius and rate of vertical migration of the bubble or cavity from a submerged explosion. To first order the maximum bubble radius R at first expansion is given by (Ref 5)

$$R \sim (B/(P_a + \rho g d))^{1/3} \quad (20)$$

where P_a is atmospheric pressure. Hydrodynamic similitude will obtain in (20) only if P_a is scaled like charge depth. The effect of atmospheric pressure, then, is to suppress the radii and, consequently, the migration rate of small bubbles over what they would have been were the pressure properly scaled. If one can presume that the normalized crater used as input for the wave solution

would be similarly affected, the wavemaking efficiency of small explosions would be enhanced relative to large ones if the pressure were scaled, and probably be more nearly proportional to the yield ratio B .

APPENDIX A

DERIVATION OF THE WAVE INTENSITY EQUATION¹

In a cartesian coordinate system where the local water depth $h(x,y)$ is a known function of position, consider a pair of adjacent rays s_1, s_2 radiating from the origin of a disturbance at point 0 (Fig A.1). Let ω and $\omega + d\omega$ be in the instantaneous positions of two adjacent frequencies propagating from 0 at their respective group velocities $V(x,y,k)$. If $E(\omega)$ is the energy per unit frequency of the source disturbance, and energy is conserved between rays, then the energy in the dark patch will always be $E(\omega)d\omega\delta\theta/2\pi$. This energy is also equal to the local wave energy within the patch:

$$E(\omega)d\omega\delta\theta/2\pi = \frac{1}{2}\rho g\eta^2 d\sigma d\xi \quad (A1)$$

where η, ρ , and g are previously defined.

Now if $\mathcal{H} = \mathcal{H}(x,y,k) = gh \tanh kh(x,y)$ is the Hamiltonian of the wave equation, then by the usual

¹ This development was kindly provided by Professor G. E. Backus, Institute of Geophysics and Planetary Physics, University of California, and will be included in a general review paper to be published by him in the near future.

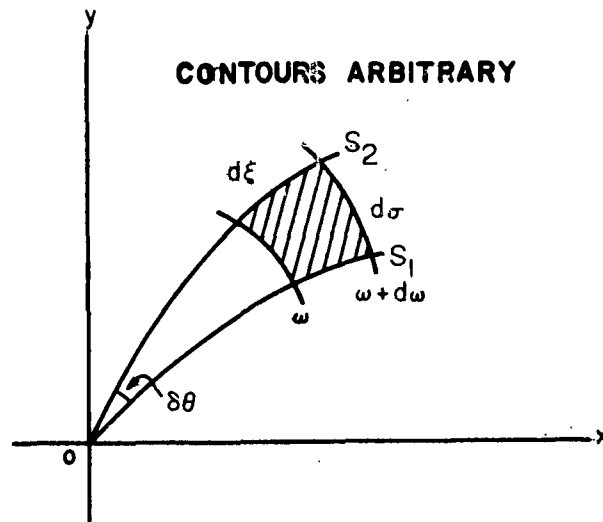


Figure A.1 Development of wave patch between two adjacent rays over arbitrary contours.

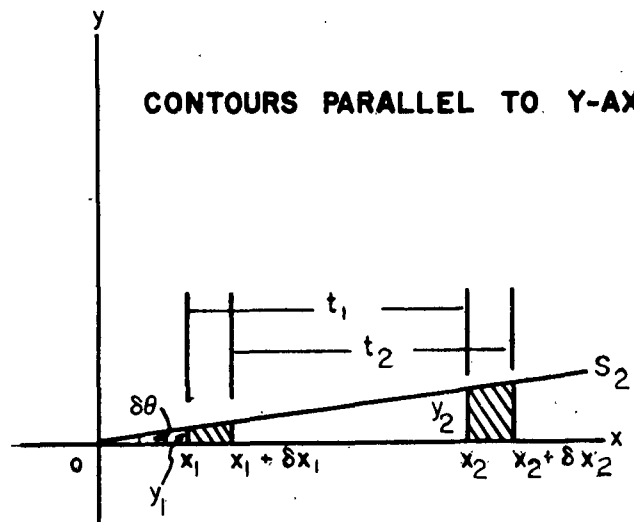


Figure A.2 Patch development for straight contours parallel to y axis.

concept of group velocity

$$V(x, y, k) = \partial \mathcal{K} / \partial k \quad (A2)$$

The wave number k can be thought of as the magnitude of a vector propagating at group velocity $V(k)$ in x, y space. Let ℓ and m be the magnitudes of the components of this vector in the x and y directions such that $k^2 = \ell^2 + m^2$. It follows from (A2) and the properties of the Hamiltonian that

$$\frac{dx}{dt} = V \frac{\ell}{k}, \quad \frac{dy}{dt} = V \frac{m}{k}, \quad \frac{d\ell}{dt} = - \frac{\partial \mathcal{K}}{\partial x}, \quad \frac{dm}{dt} = - \frac{\partial \mathcal{K}}{\partial y} \quad (A3)$$

Now along a ray $\mathcal{K}(x, y, k) = \omega = [gk \tanh kh(x, y)]^{\frac{1}{2}} = \text{const.}$, so that $k(x, y, \omega)$ is everywhere known. Define a parameter ϵ by $dt = k d\epsilon / V$. Hence $d/dt = (V/k) d/d\epsilon$ and thus equations (A3) can be expressed in terms of an 'elastic' time base linked to real time through V and k :

$$\frac{dx}{d\epsilon} = \ell, \quad \frac{dy}{d\epsilon} = m \quad (A4)$$

$$\frac{d^2 x}{d\epsilon^2} = \frac{\partial}{\partial x} \left[\frac{k^2}{2} \right], \quad \frac{d^2 y}{d\epsilon^2} = \frac{\partial}{\partial y} \left[\frac{k^2}{2} \right]$$

Equations (A4) are the analogue equations of motion of a unit particle in the field of a potential k . Similar

equations have been derived by Eckart (Ref 6) in discussing the ray-particle analogy, where l and m are the analogue velocities in the x and y directions, and ϵ is analogue time.

We wish now to apply these results to the conservation of energy within the patch given by equation (A1). In the special case where the path s_1 can be chosen normal to the bottom contours, $\partial\mathcal{K}/\partial y = y = 0$, $\mathcal{K}[\mathbf{x}, k(\mathbf{x})] = \omega$, and $d\mathbf{x}/dt = V[\mathbf{x}, k(\mathbf{x}, \omega)]$. This situation is shown in Figure (A.2). Let \mathbf{x}_1 and $\mathbf{x}_1 + \delta\mathbf{x}_1$ be the positions of ω and $\omega + d\omega$ at some time following the disturbance at 0, and let \mathbf{x}_2 and $\mathbf{x}_2 + \delta\mathbf{x}_2$ be their positions at a later time. The elapsed time t_1 for ω to propagate along s from \mathbf{x}_1 to \mathbf{x}_2 will be

$$t_1 = \int_{\mathbf{x}_1}^{\mathbf{x}_2} \frac{d\mathbf{x}}{V} \quad (\text{A5})$$

and the time t_2 for $\omega + d\omega$ to propagate from $\mathbf{x}_1 + \delta\mathbf{x}_1$ to $\mathbf{x}_2 + \delta\mathbf{x}_2$ will be, approximately,

$$t_2 = t_1 + \frac{\delta\mathbf{x}_2}{V_2} - \frac{\delta\mathbf{x}_1}{V_1} + d\omega \frac{\partial t}{\partial \omega} \quad (\text{A6})$$

where V_1 and V_2 are the group velocities near \mathbf{x}_1 and

x_2 . But the last term in (A6) can be written

$$d\omega \frac{\partial t}{\partial \omega} = - d\omega \int_{x_1}^{x_2} \frac{\partial V / \partial k}{V^2} \left[\frac{\partial k}{\partial \omega} \right] dx = d\omega \int_{x_1}^{x_2} \frac{\partial}{\partial k} \left[\frac{1}{2V^2} \right] dx \quad (A7)$$

Now, taking x_1 at the source ($\delta x_1 = 0$), setting $t_1 = t_2$, and combining (A6) and (A7), one obtains

$$\frac{\delta x_2}{d\omega} = - V_2 \int_0^{x_2} \frac{\partial}{\partial k} \left[\frac{1}{V^2} \right] dx \quad (A8)$$

which gives the change in patch length with distance traveled in the x direction.

The y axis is parallel to the contours and therefore $m = \text{constant}$ in (A4). Hence along the path s_1

$$y_2 = y_1 + m \int_{\epsilon_1}^{\epsilon_2} d\epsilon \doteq y_1 + m \int_{x_1}^{x_2} \frac{dx}{k} \quad (A9)$$

But if x_1 is at the origin, $y_1 = 0$, and $m = k_0 \delta \theta$, where k_0 is the wave number at the origin. Equation (A2) then becomes

$$y_2 = \delta \theta k_0 \int_0^{x_2} \frac{dx}{k} \quad (A10)$$

Now from Figure A.1 $d\xi = \delta x_2$, $d\sigma = y_2$, and therefore (A1) can, upon rearranging terms, be written

$$\frac{E(\omega)}{\pi \rho g} = \eta^2 \left[k_0 \int_0^{x_2} \frac{dx}{k} \right] \left[-V_2 \int_0^{x_2} \frac{\partial}{\partial k} \left[\frac{1}{V^2} \right] dx \right] \quad (A11)$$

which is the same as equation (7) Section 4.3.

REFERENCES

1. R. R. Soule, W. W. Perkins and E. A. Schuert; "An Investigation of the Radiological Effects from Underwater Nuclear Explosions Using 10,000-Pound High-Explosive Charges as Models"; August 23, 1962; U. S. Naval Radiological Defense Laboratory, San Francisco, California; Confidential.

2. Herbert C. Kranzer and J. B. Keller; "Water Waves Produced by Explosions"; Journal of Applied Physics, March 1959, Vol 30, No. 3, Pages 398-403.

3. Wm. G. Van Dorn; "The Source Motion of the Tsunami of March 9, 1957, as Deduced from Wave Measurements at Wake Island"; Proceeding Tsunami Symposium, 10th Pacific Science Congress, in press.

4. J. N. Strange, C. W. Denzel and T. I. McLane; "Cratering from High-Explosive Charges, Analyses of Crater Data"; Tech. Report 2-547 #2, June 1961; U. S. Army Waterways Experiment Station, Vicksburg, Mississippi.

5. Conyers Herring; "Theory of the Pulsations of the Gas Bubble Produced by Underwater Explosions"; Underwater Explosion Research, 1950, Vol II, "The Gas Globe", Page 77; Office of Naval Research.

6. Carl Eckart; "The Ray-Particle Analogy";
Journal of Marine Research, October 1950, Vol IX,
No. 2, Pages 139-144.